UCRL-17711

cy. 2

University of California

Ernest O. Lawrence Radiation Laboratory

A FIELD ION MICROSCOPE STUDY OF THE Ta-Mo SYSTEM

Nathapet Varadachari Durai Raghavan

August 1967

TWO-WEEK LOAN COPY

This is a Library Circulating Copy which may be borrowed for two weeks. For a personal retention copy, call Tech. Info. Division, Ext. 5545

RECEIVE
LAWRENCE
RADIATION LABORA
OCT 17 196
LIBRARY AND
DOCUMENTS SECTION

UCRL-17711 Cy. 2

DISCLAIMER

This document was prepared as an account of work sponsored by the United States Government. While this document is believed to contain correct information, neither the United States Government nor any agency thereof, nor the Regents of the University of California, nor any of their employees, makes any warranty, express or implied, or assumes any legal responsibility for the accuracy, completeness, or usefulness of any information, apparatus, product, or process disclosed, or represents that its use would not infringe privately owned rights. Reference herein to any specific commercial product, process, or service by its trade name, trademark, manufacturer, or otherwise, does not necessarily constitute or imply its endorsement, recommendation, or favoring by the United States Government or any agency thereof, or the Regents of the University of California. The views and opinions of authors expressed herein do not necessarily state or reflect those of the United States Government or any agency thereof or the Regents of the University of California.

Research and Development

UCRL-17711

UNIVERSITY OF CALIFORNIA
Lawrence Radiation Laboratory
Berkeley, California

AEC Contract No. W.7405-eng-48

A FIELD ION MICROSCOPE STUDY OF THE Ta-Mo SYSTEM

Nathapet Varadachari Durai Raghavan

(Ph.D. Thesis)

August 1967

A FIELD ION MICROSCOPE STUDY OF THE TANTALUM-MOLYBDENUM SYSTEM

Nathapet Varadachari Durai Raghavan

Inorganic Materials Research Division, Lawrence Radiation Laboratory,
Department of Mineral Technology, College of Engineering,
University of California, Berkeley, California

August 1967

ABSTRACT

A field ion microscope study of the tantalum-molybdenum system has been carried out at liquid hydrogen temperatures. The purpose of this investigation was twofold; the first being to increase the knowledge on the field ion microscopy of alloys with particular emphasis on how the solute affects the field ionization and field evaporation characteristics of the solvent atom, and the second being to categorize the segregation effects that become important at the high concentration levels to make the alloys brittle.

For this purpose, a field ion microscope fitted with a cryo-tip that generates a small volume of liquid hydrogen was built. Micrographs have been obtained from three alloys of the composition Mo-8 Ta, Mo-50 Ta and Ta-12 Mo and from the two pure metals. The field ion specimens were obtained from crystals grown in an electron beam zone refiner by a combination of swaging and cold rolling or repeated spark cutting.

The Ta-Mo alloy micrographs obtained show far more irregularity than those from W-Mo alloys. Physical and electronic factors have been shown to affect the nature of alloy micrographs. Field ionization and field evaporation processes in alloys have been discussed. The size differences in the two species forming the alloys have been suggested to be responsible for the presence of bright spots. The greater regularity of the Mo-8 Ta

micrographs over those from Ta-10 Mo has been shown to be in accord with predictions based on field evaporation from dilute alloys and the unexpected large difference in the regularity has been accounted for by considering the polarization and heat of solution terms in the field evaporation equation.

Computer simulation of images from random and clustered alloys has been performed on the assumption that solute atoms do not participate in image formation. The far too great regularity of such computed images indicates that the total invisibility criterion is an oversimplification. A band structure results when deviations from randomness become appreciable in the clustered alloy. Contrast to be expected from a demixed alloy in the Ta-Mo system has been discussed but the available experimental evidence did not reveal such contrast effects. It has been concluded that the width of such demixed zones probably exceeds 1000 Å. However a tendency for local clustering on the [200] planes was observed in the Ta-50 Mo alloy.

TABLE OF CONTENTS

1. INTRODUCTION 1

1.1 Field Ion Microscope 2

1.1.1 Image Formation in the Field-Ion Microscope 2

1.2 Work on Alloys 3

1.3 Choice of a System 5

2. EXPERIMENTAL PROCEDURES 7

2.1 Low Temperature Microscopy 7

2.1.1 Cryotip 7

2.2 Field Ion Microscope 8

2.2.1 Description of the Apparatus 8

2.2.2 The Pulse Generator 10

2.3 Specimen Preparation 11

2.3.1 Growth of Alloy Rods 11

2.3.2 Preparation of Wires 12

2.3.3 Preparation of Field Ion Specimens 13

2.4 Operation of the Microscope 14

3. RESULTS 15

3.1 Tantalum-Molybdenum System 15

3.2 Work on Pure Tantalum 15

3.3 Work on Molybdenum 16

3.4 Work on Mo-8Ta Alloy 17

3.4.1 Mo-8Ta at 77°K 17

3.4.2 Mo-8Ta at Liquid Hydrogen Temperature 18

3.5 Work on Ta-10Mo Alloy 20

3.6 Work on Ta-50Mo Alloy 21

4. DISCUSSION 23

4.1 General Features 23

4.1.1 Comparison with W-Mo System 23

4.1.2 Effect of the Second Constituent 25

4.2 Field Ionization in Ta-Mo Alloys 26

4.3 Polarization Effects 28

4.3.1 Polarization in Pure Metals 29

4.3.2 Polarization in Alloys 30

4.4 Field Evaporation 30

4.4.1 Field Evaporation Equation for Alloys 31

4.4.2 Factors Affecting Field Evaporation in Alloys 34

4.4.3 Field Evaporation of Ta-Mo Alloys 35

4.4.4 Extension to Other Systems 37

4.4.5 Field Evaporation from Concentrated Alloys 37

4.5 Image Contrast in Alloys 38

4.5.1 A Single Criterion for Field Ionization and Field Evaporation Processes in Alloys 38

4.5.2 Computer Simulation 39

4.5.3 Random Alloys 41

4.5.4 Clustered Alloys 43

4.5.5 Demixed Alloys 45

4.6 Distinguishing Between Atomic Species 46

4.7 Summary of the Results 49

5. CONCLUSIONS 51

ACKNOWLEDGEMENTS 53

REFERENCES 54

APPENDIX 1:

Determination of the Sign of the Burgers Vector from Field Ion Micrographs 56

APPENDIX 2

Contrast from Dislocation Loops 59

Determination of the Burgers Vector of the Loop... 60

Determination of the Nature of the Loop..... 60

FIGURES 61

1. INTRODUCTION

When atoms of two or more elements are able to share with changing proportions and various sites of a given crystal structure, a solid solution is formed. This concept of solid solution was introduced by Mattiessen in 1860 but did not become generally recognized until the advent of the Gibbs phase rule. After these initial formulations, few developments in the theory of solid solutions occurred until x-rays were applied to the study of metal structures. Since that time, the development of the theory of solid solutions has advanced rapidly. Hume-Rothery and Raynor were the first to set forth the factors which control the structure and properties of solid solutions. The electron theory of metals developed by Mott and Jones, Wigner and Seitz, and Slater and others, has also been effectively used to formulate the structure of solid solution alloys.

The presence of solute atoms in the solvent matrix leads to certain irregularities in the crystal both electronic and structural. The electronic disorder arises from the fact that the electronic charge distribution is no longer truly periodic in the crystal when solute atoms are present. Structural disorders can arise from the differences in size between solute and solvent atoms which produce the Huang effects. The atoms, thus, no longer reside on the average lattice sites.

The electron theory of alloys can be described by saying that an alloy will assume that type of crystal structure in which there are enough low energy states to accomodate all of the electrons in the crystal. Sivertsen and Nicholson[1] have discussed the principal factors that allow the description of electronic structure of the alloy. Since it is the

modified electronic structure of the surface of the alloy, which is imaged in the field ion microscope (the next section deals with this image formation) the field ion microscope is becoming a valuable tool in the study of alloys.

1.1 Field Ion Microscope

From the beginning it has been the aim of the microscopists to see the very small. For a hundred years the optical microscope has served to look into the microstructure of metallurgical materials. In the last two decades more powerful techniques involving x-ray and electron microscopy have given us a keen understanding of the relation between structure and properties. These have a much improved resolution over the optical microscope, but still fall short of resolving individual atoms. This logical limit to microscopy has been achieved with the advent of the field ion microscope invented by Müller in 1951.

1.1.1 Image Formation in the Field-Ion Microscope

A schematic drawing of the microscope is given in Fig. 1. Gas molecules, generally helium, at a low pressure of 1-5μ arrive at a tip maintained at a positive potential of a few kV. Upon collision with the tip surface they lose part of their kinetic energy and if the rebound energy is too small the gas atom is trapped within the region near the surface of the tip. If it does, it will lose further energy on each bounce and proceed to hop over the surface of the metal until, after having been slowed down in a sequence of up to several hundred contacts, they lose an electron by tunneling. This process is known as field ionization. The ion formed is accelerated by the field and travels in a radial direction towards the phosphor screen where it gives rise to

clear visible dots. A schematic view of image formation in the field ion microscope is given by Fig. 2.

If the field on the surface atoms of the tip is high enough then they can be evaporated as ions. This process is known as field evaporation. Field evaporation constitutes the strength of field ion microscopy since it allows clean atomic surfaces to be looked at and since it reveals the bulk structure of the specimen by careful removal of atomic layers.

The field ion microscope is capable of a resolution of 2-3Å and therefore can display the atomic arrangement on a metal surface. The microscope is thus ideally suited for investigations in which the behavior of atoms in a metal crystal is to be considered. In particular it has shed valuable information in the study of lattice imperfections, structure of metals and alloys, and the dynamics of radiation damage. Valuable information has been mostly obtained from pure metals, the micrographs of which are characterized by extreme regularity.

1.2 Work on Alloys

Field ion microscopic studies of alloys, however, has progressed at a much slower pace. Except in the case of ordered alloys, the ion images from alloys are extremely irregular. A significant limitation imposed by such a lack of crystallographic regularity is that it is very difficult to recognize and determine the nature of any lattice defects present.

In the past, two systems, namely the W-Mo system and the W-end of the W-Re system, have been studied quite extensively. Caspary and Krautz,[2] who investigated the W-Mo system, obtained micrographs from alloys containing 25, 50 and 75% Mo, and compared them with those of pure W and Mo. The micrographs were found to be quite regular though the irregularity increased towards the Mo end. They concluded that the random surfaces are due to preferential evaporation of Mo.

Ralph and Brandon,[3] who studied the W-end of the W-Re system, looked at two single phase alloys, viz., W-5 a/o Re and W-26 a/o Re and a two-phase alloy containing 34 % Re. The single-phase concentrated alloy was found to yield very irregular images. The two-phase alloy was shown to exhibit contrast due to the σ-phase. They also presented evidence to suggest that Re atoms tend to cluster and advanced a method to distinguish between the atomic species.

Work on individual alloys has been conducted to understand specific phenomena such as field evaporation. DuBroff and Machlin[4] studied the field evaporation and imaging characteristics of dilute solid solutions of gold, cobalt, nickel, tungsten, and palladium in platinum. They interpreted the vacancies observed on high index planes to arise out of preferential evaporation of solute atoms or of solvent atoms or of both.

All previous work on alloys has thus resulted in the formulation of these two questions:

1. How does the solute atom affect the field ionization and field evaporation of the solvent atoms?

2. Is it possible to distinguish between the atomic species?

Answers to these questions are at best only partially known though theories and methods have been put forward. A deeper understanding of the basic processes of field ion microscopy as well as a vindication (or a refutal) of the theories is, however, possible only with more data on alloys. Furthermore, the process of field evaporation which enables a study to be made of the bulk structure of materials can be effectively used to determine the distribution of the two atomic species in an alloy. It is thus possible to detect any tendency for deviations from random distribution. Evidence has thus been obtained to show that the Re atoms in

W-26 Re alloys tend to cluster.[3] Controlled field evaporation in such cases will further indicate the extent of such zones and it is then possible to relate the mechanical properties of the alloy to the local structure. It was therefore decided to investigate an alloy system in which these considerations can be important, viz the Ta-Mo series[7] for which a previous investigation by techniques other than FIM indicated that these solid solutions are demixed.

1.3 Choice of a System

The previous section on image formation shows a serious limitation of the field ion microscope. It is evident that successful field ion microscopy is possible only for those metals where the ionization field is lower than the evaporation field. In most metals, field evaporation occurs below the threshold field of ionization and only refractory metals give stable helium ion images. Attention was thus directed towards the four metals of Groups VB and VIB, viz., Nb, Ta, Mo and W. In addition to their refractoriness, their alloy systems possess interesting mechanical properties. Of the six possible binary alloy systems of these four metals only those in the same group, viz., Nb-Ta and Mo-W are ductile at all alloy compositions. The rest show cleavage behavior at high alloy concentrations. As mentioned before, the W-Mo system, belonging to the ductile group has been studied extensively. The Ta-Mo system, belonging to the other group, was therefore chosen since considerable information on its alloys is available.[5] In addition to the pure metals Ta and Mo, three alloys Mo-8 Ta, Mo-50 Ta, and Ta-10 Mo have been studied.

The use of low temperatures in the range of 77°K has been the normal practice in field ion microscopy. To obtain high resolution micrographs it is, however, necessary to work at lower temperatures since the resolution

δ is proportional to the half power of T. Working at lower temperatures confers other advantages as well. The working range, which is the region between the best imaging voltage and the field evaporation voltage, is widened at low temperatures and therefore operation below 30°K becomes mandatory in most cases. Besides, the increased resistance to plastic flow at low temperatures reduces the possibility of specimen deformation due to the electrostatic field and cryogenic pumping of the system reduces the contamination rate.

Both Ta and Mo are not imaged satisfactorily at 77°K. For Ta, the resolution is poor and for Mo, the working range is extremely short. It was therefore decided to conduct the field ion microscopy of the Ta-Mo system at temperatures below 30°K.

2. EXPERIMENTAL PROCEDURES

2.1 Low Temperature Microscopy

The present study was conducted in a stainless steel microscope fitted with a liquid hydrogen cryotip. The advantages of working at low temperatures have already been enumerated in the previous section. Temperatures lower than 30°K are obtained by using liquid neon (27°K), liquid hydrogen (21°K), and liquid helium (4°K). The use of liquid neon, at a cost of approximately $100.00 per liter is prohibitively costly; liquid helium, on the other hand, poses problems in the design of microscopes since the losses due to its extremely rapid evaporation have to be minimized. Liquid hydrogen, in spite of the safety hazards associated with its use, has been most commonly used. In the present study, a commercially available equipment, known as the cryotip, has been used as a source of liquid hydrogen. In the cryotip, a small volume (2-5 cc) of liquid hydrogen is generated and maintained in a sealed portion of the microscope, thereby eliminating storage, handling and transfer. The explosive hazards attendant on the use of liquid hydrogen are thus avoided completely.

2.1.1 Cryotip

The liquefier, a schematic diagram of which is given in Fig. 3, is an open-cycle Joule-Thomson refrigerator and has two separate circuits, one each for the nitrogen and the hydrogen gases. The main purpose of the nitrogen circuit is to provide the precooling of the hydrogen below its inversion temperature (160°K) thereby allowing the Joule-Thomson cooling of the hydrogen gas to occur. Because of the recuperative effect from the two heat exchangers, all lines both into and away from the heat exchanger

are essentially at room temperature. The copper block (see Fig. 6) is the only portion of the heat exchanger assembly which is at liquid hydrogen temperature. However, by regulating the gas pressure above the liquid pool, known as the hydrogen back pressure, all temperatures in the range of 77°K to 18°K can be obtained. The cool-down time depends upon, a) the refrigeration available, b) specimen load, and c) direct heat leak. Table I gives typical cool-down times for a few combinations of hydrogen and nitrogen pressures.

Table I Typical cool-down times for a few combinations of hydrogen and nitrogen pressures in the hydrogen liquifier.

Initial pressure before inlet of gases	N_2 pressure (psi)	H_2 pressure (psi)	Formation time (mins)	
			liq.N_2	lig.H_2
1×10^{-5}	1400	1000	8	35
1×10^{-5}	1500	1100	6	30
1×10^{-5}	1500	1200	6	25

2.2 Field Ion Microscope

2.2.1 Description of the Apparatus

The microscope was designed so that the cryotip can be fitted onto it in a facile manner. The microscope consists of three parts, a) the gas supply system, b) the vacuum system, and c) the microscope head. A schematic view of the overall set-up is given in Fig. 4. Figure 5 is a photograph of the entire microscope with all units used in experiment. The gas supply system has facilities for the use of two image gases; one is invariably helium, the other can be neon or hydrogen. The image gases

which are of research grade (99.9995% purity) are contained in liter bottles at 80 psi and can be bled into the gas supply system after evacuation of the system, by means of a Granville-Phillips leak valve. The vacuum system, which pumps both the gas supply system and the microscope, consists of a rotary pump backing a 2-inch oil diffusion pump with a stainless steel liquid nitrogen trap. The vacuum joints between components are made of copper O-rings. The ultimate vacuum is read on a Veeco ionization guage.

The microscope head is made of stainless steel and has three openings, a 4-1/2-inch opening for the cryotip, a 5-inch opening for the screen and a 1-1/2-inch opening for connecting to the pumping system. Two types of specimen holders have been used. One is the cryotip itself with provision for attaching the specimen. The other is a specimen holder made of glass which has been used to study specimens at liquid nitrogen temperature.

Figure 6 shows a schematic view of the microscope head with the cryotip sealed off from the surroundings. The copper block at the bottom end of the cryotip is attached to the specimen through an intermediate alumina block 1/4-inch in thickness. The alumina, which is threaded onto the copper block, provides insulation between the tip at high potential and the grounded cryotip. At the same time, by virtue of its high thermal conductivity, the alumina also serves to cool the specimen to liquid hydrogen temperatures fairly rapidly. The high tension lead, which is a 1/8-inch thick tungsten wire, is brought into the chamber insulated by means of a glass tube and is connected to the specimen through a thin wire. Early results showed that good thermal contact between the alumina and copper blocks is essential for the

specimen to reach temperatures near 21°K and be maintained there. This was achieved by coating the well-cleaned bottom surface of the copper block with a low melting gallium-indium eutectic alloy and by vapor depositing pure indium on the top surface of the alumina block before bringing the two surfaces together.

The other specimen holder, made of glass, is attached to a flange by means of a Kovar seal and can be fitted to the microscope head. Leaks through the Kovar seal giving in at liquid nitrogen temperatures have given considerable vacuum problems and it is advisable to use copper seals. The specimen holder can be filled with liquid nitrogen. It is thus possible to look at specimens at 77°K.

The screen is a 5-1/2-inch diameter, 1/4-inch thick pyrex disc. A transparent tin oxide layer deposited on its surfaces helps to keep the screen at ground potential. The phosphor is deposited on the screen using a technique described by Gomer.[6]

2.2.2 The Pulse Generator

An attractive technique in field ion microscopy is controlled field evaporation, whereby surface atoms can be removed by application of pulses of electrostatic field greater than the evaporation field. Particularly, for studies such as examination of defects or preferential evaporation in alloys, it is desirable to control precisely the rate of field evaporation and to maintain a sharp image during the evaporation process. This can be readily accomplished by superimposing onto the best imaging voltage a repetitive pulse or single pulse voltage with an amplitude just sufficient to cause field evaporation.

A Velonex pulse generator Model 350 provided voltage pulses with desired amplitude, width, and frequency. The pulse shape is approximately square with a rise time of 10^{-8} sec. and a fall time of 10^{-7} sec. The pulse width can be adjusted from 0.1 μ sec. to 200 μ sec. The typical pulse amplitude was 1-2 kV in the field evaporation process. The schematic diagram of the field evaporation pulsing unit is shown in Fig. 7.

2.3 Specimen Preparation

The specimen preparation is the single most important step in successful field ion microscopy. Tantalum and molybdenum are available in the form of 10 mil wires and can therefore be directly used for preparing field ion specimens. In the case of the alloys, the alloy crystals were first obtained as rods grown in an electron beam zone refiner.

2.3.1 Growth of Alloy Rods

The electron beam zone refiner not only provides a convenient method for the growth of crystals of high melting point but also ensures high purity. The purification by the refiner results from the high energy of the electron beam which is capable of decomposing the most stable compounds of the refractory metals with the common interstitials such as oxygen, carbon, nitrogen, and hydrogen. The alloy crystals were prepared by melting together proper combinations of tantalum and molybdenum rods of different diameters. Complete mixing of the alloy constituents, thereby assuring a homogeneous crystal, was achieved by giving a number of passes, generally four, and by melting from top and bottom on alternate passes. To check the homogeneity of the alloy, a disc of an alloy rod was mounted into an

electron microprobe analyzer, along with pure Ta and pure Mo. Counts were taken at intervals of 100 μ. The composition deviations were found to be less than 3%. The exact compositions of the alloy crystals were then determined by measuring the lattice parameters and by comparing the present data with those for the Ta-Mo alloy system measured previously (Fig. 8a).[7] An x-ray diffractometer was employed to measure the lattice parameter and the alloy powders were prepared by filing the rods carefully. The lattice parameter computed from the high angle lines was plotted against $\sin^2\theta$ and extrapolated to 1. The compositions of the alloys grown were determined to be Ta-10 a/o Mo, Mo-8 a/o Ta, and Ta-47 a/o Mo. The Ta-47 a/o Mo alloy, for convenience, will from now on be referred to as the Ta-50 Mo alloy.

2.3.2 Preparation of Wires

Field ion specimens are generally prepared from thin wires and the reduction of the alloy rods to such wire form poses problems. While the concentrated alloy is inherently brittle, even the normally ductile dilute alloys were found to be extremely brittle under the compressive and twisting conditions of swaging. The two end alloys, however, were successfully reduced by a combination of swaging and cold rolling. The rods were jacketed in a stainless steel tube and swaged in small reductions to 50 mil diam. wires. The outer jacket was then stripped off and the wires were cold rolled to give 7-10 mil strips. The strips were then sheared at 7-10 mil intervals to give wires of uniform cross section. The wires thus obtained were annealed for 24 hrs in an annealing furnace at 2000-2200°C in helium atmosphere. The helium used was of 99.9995% purity obtained in a helium purifier. Pure Ta was used as the resistor in the furnace.

This method was found not to be applicable for the Ta-50 Mo alloy which is too brittle. Spark cutting has proved to be the only method that is fairly successful. The cylindrical rod, 1/4-inch diam., was first sectioned on the spark cutter longitudinally. The strips obtained were cut at uniform intervals to obtain wires of square cross sections. Twenty mil thick wires were found to be of the optimum dinension. Thinner wires crumbled while spot welding to the nickel wire of the specimen holder preparatory to electropolishing, whereas thicker wires took too long for polishing.

2.3.3 Preparation of Field Ion Specimens

Tips of a few hundred Å radius are necessary for ion imaging at low enough potentials when the resolution is high. Such fine tips suitable for field ion microscopy are obtained by electropolishing. Mo and Mo-8 a/o Ta alloy are both conveniently polished in a 20% aqueous solution of KCN at 5-10 volts AC. The double layer method, whence the specimen is dipped in a 2mm layer of the electrolyte floating on top of a bath of carbon tetrachloride, has been adopted. Specimen preparation by this method has been found to be very fast and reproducible. The polishing of Ta, Ta-10 a/o Mo, and Ta-50 a/o Mo is considerably more difficult. These were electropolished in an electrolyte consisting of 4 parts of HF, 2 parts of H_2SO_4, 2 parts of H_3PO_4, and 1 part of acetic acid to which some HNO_3 was added. An iridium cathode was used and polishing was done at 10-15 volts dc, 0.1-0.15 amps, and -10 to -20°C. The low temperature was meant to reduce oxygen and hydrogen pickup. Normally, the impurity pickup during polishing is not a serious problem in field ion microscopy since under the high field conditions near the tip, the impurities are ionized and removed. In the case of bcc metals however, the brittleness associated with the

presence of small amounts of impurity makes it necessary to minimize such diffusion of interstitials. The method is not reproducible; in particular Ta-10 a/o Mo specimens gave extra difficulty while polishing. The tips were either blunt or swiftly destroyed by flashing in the microscope apparently due to oxygen embrittlement during polishing.

Polished specimens were looked at with an optical microscope for sharpness and absence of multiple tips.

2.4 Operation of the Microscope

The specimens were first observed at liquid nitrogen temperature using the dummy specimen holder. This served to determine whether the specimens gave large streak-free images. Only good tips were transferred to the cryotip specimen holder. After attaching the cryotip to the microscope head, the system is evacuated to a vacuum of 1×10^{-5} mm Hg or better. The nitrogen gas and the hydrogen gas circuits are opened to the cryotip, carefully following the instructions given in the cryotip manual. In about 30 minutes, liquid hydrogen is formed. Because of the large thermal capacity of alumina, it is best to wait for at least 15 minutes so that the specimen will reach temperatures near 21°K. Research grade helium is let in at 6×10^{-4} pressure (1×10^{-4} on the ion guage) and the voltage increased gradually. The image is observed either directly or on a 10× ocular telescope. Since the image intensity is low, it is necessary to have the fastest possible combinations of film and camera lens. A Canon Camera with a f.0.95 lens and suitable extension rings for close-up work was used in conjunction with Kodak Tri X film (AsA 300). The film is developed in acufine. Because of the large aperture optics, perfect focusing is essential and is achieved by performing a focusing series and locking the camera at the best focus.

3. RESULTS

3.1 Tantalum-Molybdenum System

Tantalum and molybdenum form completely miscible solid solutions with each other as do all the other binary alloys of the four refractory metals Nb, Ta, Mo, and W. The phase diagram of this system is given as Fig. 9. Previous work on the Ta-Mo system[7] has shown that alloys in the composition range of Mo-19Ta to Mo-58Ta cleave on the {100} planes. X-ray intensity measurements indicated that there exist deviations from random solid solution in these alloys. It was suggested that cleavage occurs due to a violation of the strain energy restrictions on the elastic coefficients in a local region of the crystal.

3.2 Work on Pure Tantalum

Figures10 and 11 are helium ion micrographs of pure Ta obtained at 77°K and 21°K, respectively. The splendid resolution of Fig. 11 clearly brings out the advantages of working at lower temperature. Since the field evaporation end form of Ta has been discussed by Nakamura and Müller[8] in detail, only the important observations, which will be useful for subsequent discussions, are being made here. Tantalum is observed to develop a large number of planes, in particular {200} which is developed poorly in W and Mo, with excellent resolution. The micrograph has a characteristic intensity distribution: the square {002} region bounded by {011} planes is bright, whereas the triangular {222} region also bounded by {011} planes is dim except for the {222} planes themselves. This intensity difference is found to be more marked with micrographs obtained at liquid nitrogen temperature. The region extending from the

{112} to {114} is found to be characterized by a random appearance brought about by a rearrangement of atoms. The prominent spots in these regions have been suggested[8] to be due to metal atoms in low coordination sites. Such sites may be stabilized under the influence of the field if the gain in polarization binding energy due to increased field penetration is greater than the loss in electronic binding energy.

3.3 Work on Molybdenum

Figure 12 is a field ion micrograph of Mo at 21°K. The number of planes appearing well developed and well resolved is considerably less than in Ta. This is to be attributed to the higher strength of the Ta lattice, as well as the poor working range of Mo. In Mo the {222} regions in particular, yield under the shear component of the field stress. Müller[9] has suggested that the dislocation loops formed as a result of this yielding, are responsible for the random appearance of the {222} planes in Mo. The dislocation loop contrast obtained in field-ion micrographs has been considered carefully by the author, Petroff, and Ranganathan. The intersection of a loop on the specimen surface results in well defined image contrast due to the two line segments, the nature of which is defined by the Burgers vector and the habit plane of the loop. A more detailed discussion of the loop contrast is given in Appendix 2. It is to be concluded that the presence of dislocation loops cannot be the primary cause for this random appearance of {222} planes in Mo. The Mo micrographs show other differences, as well, from the Ta patterns. The intense square region of Ta is dim in Mo while the weak regions around {222} in Ta are exceedingly bright. The presence of low coordination sites identified by their brightness is not observed. The [001] zone decoration line running

between {011} and {002} planes, totally absent in Ta, is observed, though not in a clear fashion as in W. Since these features arise as a result of the field penetration it is to be concluded that polarization effects are much stronger in Ta than in Mo; this point is discussed at length in Sec. 4.3.

3.4 Work on Mo-8Ta Alloy

Of the alloys of the Ta-Mo system studied, Mo-8Ta gives the most regular images. Figure 13 is a typical field ion micrograph from a Mo-8Ta tip. The orientation is an unusual ⟨100⟩ compared to the normal ⟨110⟩ texture developed by Ta, Mo, and W. This is obviously due to the severe deformation introduced during the reduction of the alloy rod to a wire and the subsequent annealing. All the specimens of this alloy, that were looked at in the microscope, exhibited the same orientation.

3.4.1 Mo-8Ta at 77°K

In view of the ease with which Mo-8Ta specimens can be prepared and the reasonably good images they cast even at liquid nitrogen temperature, this alloy was studied both at liquid nitrogen and liquid hydrogen temperatures. Figures 14 (a-c) are a series of micrographs taken at 77°K with considerable field evaporation in between.

Figure 14 (a) is a helium ion image at 9 kV. The (200) which appears first as a result of earlier field ionization is found to be absent. This could be due to the presence of a pit. Continued field evaporation resulted in a shift of the image to Fig. 14 (b). The {110} planes are rather poorly imaged but the (200) plane at the center has come into existence. Figure 14 (c) is the image taken at the best imaging voltage, obtained after further field evaporation. The micrograph brings out nicely the ⟨100⟩ orientation of the pattern. It is apparent that the resolution

is quite poor except in isolated regions near the {110} and {222}. This is in accordance with the behavior to be expected from a Mo-based alloy, since the working range for Mo at liquid nitrogen temperature is quite low. In fact the image obtained is fairly well resolved in comparison to that of a pure Mo micrograph and this is believed to be a result of the addition of tantalum. There is considerable solid solution strengthening when Ta is added to Mo up to 18%, (Fig. 8), and the increased yield strength enables the lattice to withstand the stresses due to the field without much plastic deformation. The slight increase in the evaporation field due to the addition of Ta possibly contributes to the improvement in image quality. Small additions of Zr or Ni which produce spectacular increases in the yield strength of Mo[10] are thus expected to result in improved micrographs even at liquid nitrogen temperature.

The characteristics of the Mo micrographs are observed to be otherwise preserved. The bright triangles bounded by {110} planes, though incomplete because of the unfavorable orientation, are present. The marked contrast of image points on either side of the ⟨111⟩ zone line passing through {011}, {112}, and {101} planes is also clearly observed.

3.4.2. Mo-8Ta at Liquid Hydrogen Temperature

Since low temperatures have the effect of increasing the working range in metals, Mo-8Ta should be expected to give superior micrographs at 21°K. Figure 15, which is a helium ion micrograph of Mo-8Ta obtained at liquid hydrogen temperature, shows that this is indeed so.

The occurrence of the typical ⟨001⟩ zone decoration line present in Mo (as also in W) establishes that the working temperature would be much lower than 77°K. The intensity difference on either side of the {112}

planes is observed to be much less marked than in the micrographs of Mo-8Ta imaged at 77°K. A similar feature can be observed in the Ta micrographs presented earlier. The role that temperature plays in the field ionization process is, however, not understood well enough to explain this. A good number of planes like {110}, {112}, {310}, and {222} are all observed to be well developed. The {222} region of Mo which generally appears with poor resolution is delineated with much better resolution in these micrographs (see Fig. 15).

A large series of pictures from this alloy tip was taken using the pulse generator with single pulses of height, 1 kV, and a duration of 30 μsec. It is clear from Fig. 15 which was obtained after about 30 pulses that controlled field evaporation leads to images of better resolution and regularity. This is possibly due to the minimizing of the lattice deformation due to large fields since the elastic stored energy in a specimen due to the applied field increases with the fourth power of the field. As Brenner[11] has pointed out, the resolution is found to be significantly greater near the edges of atom planes so that in a large diameter plane only the edge atoms are visible.

All the Mo-8Ta micrographs obtained in any evaporation sequence show the common features of a Mo micrograph. However, in the usually less intense square described in Sec. 3.2, some bright spots are observed and similarly in the intense triangle bounded by {110} planes there are some weak spots. In the section on the distinguishing between atomic species, this feature has been used to suggest a method to distinguish Mo from Ta atoms. Thus in Fig. 16 (a), the group of atoms marked A can be identified to be all Mo atoms. In Fig. 16 (b) which was obtained by a single pulse all those atoms are seen to have been removed by evaporation.

Figures 17 (a) and (b) which were also obtained in consecutive field evaporation pulses similarly show the evaporation of a group of atoms tentatively identified as Ta atoms.

The presence of dislocations has been frequently observed in this alloy. Continued field evaporation was rarely found to change the pole through which a dislocation emerged on the surface, indicating that the dislocation line is parallel to the wire axis. Figure 18 is an example of a micrograph showing dislocation contrast on the (130) plane. Dislocation contrast in field ion images has been discussed by Ranganathan.[12] When the dislocation line does not lie on the plane of observation, $\vec{g}$, we consider $\vec{g} \cdot \vec{b}$ which gives the component of the Burgers vector normal to the plane. (The case where the dislocation line lies on the plane is rare and can be dismissed from consideration.) This component can be either zero or equal to an integral number of interplanar spacings. In the first case, i.e., if $\vec{g} \cdot \vec{b} = 0$ net plane rings will appear as rings. If $\vec{g} \cdot \vec{b} = n$ an n-leaved spiral results. A double spiral is observed to be present in Fig. 18 and the application of the above $\vec{g} \cdot \vec{b}$ rule assuming that it is a perfect dislocation gives the Burgers vector to be a/2 [111] or a/2 [11$\bar{1}$]. It is possible to assign, in particular cases, a sign to this Burgers vector from the nature of the spirals. The relation of the sign of the Burgers vector to this sense of spirals in field ion images has been discussed in Appendix 1. The disturbance of atoms in region A of the microscope seems to be due to the core of the dislocation.

3.5 Work on Ta-10Mo Alloy

Figure 19 (a) shows a helium ion micrograph from a Ta-10Mo tip. The addition of 10 a/o of molybdenum is seen to have disturbed the field ion image extensively. Since the addition of Mo also results in considerable

strengthening of Ta (Fig.8b) the appearance of such random surfaces cannot be due to lattice deformation by the field stress. The excellent resolution in the {110} and {130} regions rule out the possibility that the specimen did not quite attain low temperatures.

The addition of Mo also results in a good number of dark regions where no imaging is apparently taking place, and which persists during field evaporation (Fig.19b). The reason for this is obscure, though preferential field evaporation is likely to be responsible. Significantly present are also a large number of bright spots which are also not removed by extensive field evaporation. The discussion in the field ionization section will show that such bright spots are to be attributed to field penetration polarization and size difference effects.

3.6 Work on Ta-50Mo Alloy

Figure 20 shows the helium ion micrograph of a Ta-50Mo tip. The micrograph is characteristic of a concentrated alloy in that only a few planes e.g., (110), (112), (222) than (310) have formed in a good manner. The image is observed to be lacking in the characteristics of pure Ta or Mo and in fact is more similar to that from W alloys. The image intensity is uniform throughout the entire micrograph. This is, however, to be expected since the composition corresponds to that of middle alloy and Ta and Mo are complementary in their image intensity relationship.

The number of spots also appear to be significantly less than would be expected from a tip of this radius. Further, almost all of the spots appear to be bright. These observations suggest that perhaps not all the surface atoms are participating in image formation, and as mentioned above, those that are giving rise to image spots are perhaps in protruded positions on the surface. It is however difficult to categorize whether

all these atoms belong to the same atomic species as happens to be the case in ordered alloys. Besides the inherent distribution of atoms in the lattice, the field ionization and field evaporation processes are also to be carefully considered for a clear understanding of the situation.

Figures 21 (a-c) are a series of micrographs from a Ta-50 specimen showing the effect of local clustering. The (200) plane in Fig. 21 (a) is found to be well developed. Figure 21 (b) was obtained by field evaporation of the surface of Fig. 21 (a), with a small pulse and it is seen that the (200) region has become considerably random. After the removal of seven more atom planes, Fig. 21(c) was obtained. The micrograph shows the appearance of a well developed (200) region. The series of micrographs obtained thus shows that this clustered region is approximately 25Å in diameter. A good number of such pictures have been observed to vary continuously in regularity, thereby providing strong evidence for the existence of such small clustered regions. This result is in accordance with the proposal of Van Torne and Thomas[7] that such deviations from randomness occur on the (200) plane in the Ta-rich Ta-Mo alloys.

4. DISCUSSION

4.1 General Features

4.1.1 Comparison with W-Mo System

Since Caspary and Krautz[2] have previously performed a similar study on the W-Mo system, it is perhaps best to compare the micrographs obtained from the two systems.

It is obvious that the ion images from the Ta-Mo system are considerably more irregular. Table II, which lists the planes that are identifiably present in the Ta-Mo alloy micrographs, well substantiates this point. This assumes greater significance in the light of the fact that the two end alloys of the Ta-Mo system studied are quite dilute compared to the two of W-Mo studied by Caspary and Krautz. An asymmetry similar to the one observed about the 50% solute in the W-Mo system can be observed to be present in the Ta-Mo micrographs as well, but the sense of this asymmetry is opposite. In W-Mo, the W-based alloys are more regular over a larger solute concentration, whereas in the Ta-Mo system it is the Mo-based alloy that is found to be more regular. It should, however, be noted that the compositions of the alloys of the two systems studied are not the same.

Though the two systems are comparable in that they form completely miscible alloys with bcc structure, previous work on the mechanical properties of the alloys of the two systems has shown that there exists considerable difference in their plastic behavior. While the W-Mo alloys are ductile at all compositions, the alloy crystals in the high concentration range of the Ta-Mo system suffer cleavage on specific crystallographic planes. This brittle behavior has been attributed to deviations from random composition which are possibly brought about by differences

Table I. List of planes appearing in field ion images of Ta-Mo alloys and W-Mo alloys[2]

Zones uvw	Planes		Mo content (a/o) of the Ta-Mo Alloys					Mo Content (a/o) of the W-Mo Alloy				
	$hk\ell$	$h^2+k^2+\ell^2$	0	10	50	92	100	0	25	50	75	100
[100]	110	2	x	x	x	x	x	x	x	x	x	x
	200	4	x	x	x	x	x	x	x	x	x	x
	310	10	x	x	x	x	x	x	x	x		x
	420	20	x			x	x	x	x			x
	510	26	x				x	x				
	530	34	x					x				
	640	52										
[111]	110	2	x	x	x	x	x	x	x	x	x	x
	211	6	x	x	x	x	x	x	x	x	x	x
	321	14	x			x	x	x	x	x		x
	431	26	x				x	x	x			x
	541	42	x					x				
[110]	110	2	x	x	x	x	x	x	x	x	x	x
	200	4	x	x	x	x	x	x	x	x	x	x
	211	6	x	x	x	x	x	x	x	x	x	x
	222	12	x	x	x	x	x	x	x	x	x	x
	411	18	x			x	x	x	x	x	x	x
	332	22	x					x	x	x	x	x
	433	34	x					x	x	x		x
	442	36	x					x	x			x
	611	38						x	x			
	622	44						x				
	552	54						x				
	644	68						x				
	662	76						x				

in atomic size of the two species.[7] It is logical to consider the same factors to be responsible for the differences in ion images from the two systems. This is discussed in greater detail in the field evaporation section.

4.1.2 Effect of the Second Constituent

It is evident that the addition of a second element is responsible for the breaking down of the regularity of the pure metal micrographs. As mentioned previously there is the overall irregularity of the images stemming from the absence of the high index planes. This, as well as the occurrence of pitted regions, is due to the preferential evaporation of one species. The atomic rings also appear jagged and this local irregularity is possibly due to the size difference effect.

The addition of an alloying element brings about changes in the ion images by its effect on the physical properties and electronic properties of the solvent. An important physical property, relevant to field ion microscopy, is the yield strength. For most bcc metals except for W and Ta, the field strength which increases as the second power of the field causes yielding in restricted areas. W and Ta are apparently strong enough to stay undeformed at their respective evaporation fields. The addition of 8% Ta considerably strengthens the Mo lattice so that the (222) regions of the Mo-8Ta are developed without the incidence of dislocation loops formed as a result of the field stress. A careful consideration, therefore, of the effect of solute can be used to obtain useful information about the distribution of the two species.

The distinct differences between the field evaporation end forms of the three refractory metals with bcc lattice - W, Mo, and Ta, have been attributed to the specific electronic structures of the metal surfaces.

In W the intensity is more or less uniform throughout. Molybdenum develops an intense triangle bounded by {110} planes and in Ta the same region is dark except for the {222} plane. As mentioned earlier, there are marked differences in the depiction of the zone decoration lines also. The intensity differences have been suggested by Muller[13] as arising out of a fairly large crystal-orientation and material-dependent reflection coefficient for an electron about to tunnel out of an imaging gas atom. We thus expect the behavior of the Ta-Mo alloy to be an averaged effect of the Ta and Mo lattices and indeed the Ta-50Mo micrograph resembles the W ones with even intensity throughout.

4.2 Field Ionization in Ta-Mo Alloys

Image formation in the field ion microscope is governed by two important processes, viz., field ionization and field evaporation of atoms. The distinct differences of the alloy micrographs from those of pure metals are therefore sought to be explained by considering what effect the solute atoms have on these phenomena. Field ionization is considered first and since it is a quantum mechanical process, knowledge of which is meager, a summary of the theory of field ionization is first presented before the conclusions that have been drawn.

As an atom approaches a metal surface, there is a probability that its valence electron will tunnel into the metal. This effect as modified by an externally applied electric field is field ionization. When the atom comes closer to the surface than a certain critical distance, X_c, ionization is no longer possible because all the electronic states below the Fermi level of the metal, to which tunneling can occur, are occupied. When a solute atom is added to the solvent matrix, it produces

a change, ΔE, in the electronic energy of the solvent. If the ionization energy of the solute atom is greater than that of the solvent, then the ion core of the solute will attract a valence electron more strongly than will a solvent atom. This will result in an accumulation of charge at the solute ion at the expense of the electronic charge distributed over the rest of the lattice. The result of such a "spilling" of even a small fraction of the electronic charge from the solvent to solute will drastically reduce the local field strength and, therefore, the field ionization rate above the solute atoms, such as to make them invisible or only partially visible. The opposite situation is expected if the ionization energy of the solvent is greater than that of the solute. It is seen that the immediate effect in either case is that the potential field will become smoothed out by the valence electron shifts. Unfortunately, the ionization potentials of the refractory metals are too poorly known to draw useful conclusions of this nature. We can, however, assume that if the nuclear charge of the solute atoms differ by only one or two from the charge on the solvent atoms, then such polarization of the conduction band near the solute will not be large enough to cause large field ionization differences by itself. We can thus conclude that in the Ta-Mo system, since the atomic number of Ta is 73 and that of Mo is 42, such field ionization differences could be large, and, as the following discussions will indicate, that the charge transfer would be from Ta to Mo.

Besides the inherent electronic nature of the solute, a purely physical factor such as the atomic size has a significant influence on the field ionization process. Results on the Ta-10Mo and Ta-50Mo alloys showed that the micrographs of these alloys are characterized by a large number of bright spots which are not removed by extensive field evaporation.

This observation suggests that these are not caused by adsorbed foreign atoms or molecules (in Ta-10Mo it can, for example, be oxygen diffused during preparation of the specimen) the binding energy of which to the matrix has been increased by field penetration polarization. On the other hand, the considerable size difference (~5%) between the two species, that results in a surface with considerable protrusion, is to be considered responsible for this effect. Above the surface protrusions the local field is enhanced and consequently the ionization rate is also increased leading to the formation of bright spots. Also it must be noted that at such protruded atoms field penetration must be higher and the effect of the increased field penetration is to reduce the critical distance x_c beyond which the field ionization of the imaging gas is permitted. The results of Tsong and Müller[14] have indicated that the ionization probability rises sharply at x_c and drops, unexpectedly fast, beyond that distance with a half width of only 1/6Å. Therefore, at a protuberant surface atom with the critical distance x_c reduced by the depth of field penetration, there is further increased ionization probability leading to a brighter image. The absence of such large numbers of spots in the micrographs of W-Mo alloys studied by Caspary seems to support this explanation.

4.3 Polarization Effects

Polarization affects the field evaporation process as expressed by the field evaporation equation,

$$Q = \lambda + \Sigma I_n - n\phi + P$$

where Q is the activation energy for field evaporation and P is the binding energy due to surface polarization. Since polarization effects

have been shown to affect the topography of field evaporated surfaces[15] it is considered before field evaporation.

4.3.1 Polarization in Pure Metals

The origin of polarization effects has been reviewed by Brandon.[16] Essentially, there are three polarization correction factors corresponding to 1) a double layer potential, 2) a dipole moment, and 3) the polarizability of surface atoms. The double layer potential is already accounted for in the field evaporation equation written above, since the measured work function ϕ has been used instead of the inner potential ϕ_o. The dipole moment is proportional to $1/q$ where q is the screening distance and is nearly the same for W, Mo and Ta. The surface polarizability correction factor P_s is given by

$$P_s = 1/2\ (\alpha_a - \alpha_i)\ F^2$$

where α_a and α_i are the polarizability of the atom and the ion core respectively and F is the field. α_a is of the order of 1-10Å^3 depending on the density of the plane and is related to the compressibility, X of the metal, since X is a measure of the electrical forces between the ion cores. α_i is simply related to the univalent radius of the ion and is commonly of the order of 0.2Å^3 so that its effect can be neglected. Thus, a large value of X indicates a large P_s. Of the three refractory metals, W, Mo, and Ta, Mo does not show the presence of atoms occupying low coordination sites. In W, such atoms are observed, which are removed by field evaporation at 77°K. In Ta, on the other hand, they persist till field evaporation at 300°K.[8] It has already been mentioned that such low coordination sites are stabilized by field penetration polarization and it can, therefore, be concluded that the polarization effects

are strong in Ta but much less so in Mo and W. This conclusion is supported by a comparison of the χ values listed in Table III, where it is seen that Ta has the largest compressibility. In accordance with this criterion, Nb which has an even higher χ than Ta should also show a strong tendency for stabilization of low coordination sites and indeed Nb micrographs show such occurrence of a large number of spots occupying metastable sites.[17]

4.3.2 Polarization in Alloys

Polarization effects in alloys can become important if the polarization term corresponding to one species is larger than the other. The effect of polarization in the field ionization of an alloy, having different polarization corrections, has already been shown to result in the occurrence of bright spots, which correspond to atoms with higher field penetration. The above discussion, therefore, leads to the conclusion that in Ta-Mo alloys, the bright spots are more likely to correspond to Ta atoms. The effect of polarization on the field evaporation process will be discussed in the next section.

4.4 Field Evaporation

Field evaporation is now well recognized to affect the nature of alloy micrographs mainly through the preferential evaporation or retention of the solute in the lattice. This approach has been recently employed by Brandon[18] in the case of field evaporation from dilute alloys. A similar viewpoint has been taken in the discussion below towards understanding the field evaporation process.

4.4.1 Field Evaporation Equation for Alloys

The field evaporation process from pure metals is now relatively well understood. Rewriting the original equation for the activation energy Q_0 for field evaporation to include the polarization corrections,

$$Q_0 = \lambda + \Sigma I_n - n\phi + P$$

where λ = sublimation energy, ΣI_n = sum of the ionization potentials, the charge of the evaporating ion being ne, ϕ = work function and P = binding energy due to surface polarization.

In the case of an alloy, we are interested in field evaporation from particular sites since these can be occupied by different species. The field evaporation equation has to be modified therefore to account for the changes in the various parameters, appropriate to the particular species. It is apparent that there are two distinct cases to be considered. The first is that of the dilute alloy, where the solute content is assumed to be small enough for solute-solute interactions to be neglected. In the second case, the solute content is appreciable enough for the solute atom to affect the evaporation of both the species. Electronically, this corresponds to the situation where the perturbations produced by the solvent atom are no longer restricted to the immediate locality of the solute, but may extend to the nearest or second nearest neighbor atoms. The case of the dilute alloys is considered first.

The activation energy Q_B' necessary to field evaporate a B atom from the surface of a dilute alloy of B in A can be calculated by considering the following cycle:

1. Evaporate a B atom

2. Ionize it n times where ne is the charge with which B is ionized in the field evaporation process

3. Return the n electrons to the matrix A.

Q_B' is therefore given by

$$Q_B' = \lambda_B + \Sigma I_n^B - n\phi_A + P(B)$$

where λ_B is the sublimation energy of B in A, and P(B) is the polarization correction appropriate to the B atom.

λ_B is approximately given by[15]

$$\lambda_B = \lambda_O^B + H_S$$

when λ_O is the sublimation energy of pure B and H_S is the heat of solution.

Since the alloy is dilute the activation energy Q_A' for evaporation of A can be equated to its activation energy Q_A° of pure A. A_A' it therefore given by

$$Q_A' = Q_A^\circ = \lambda_A^\circ + \Sigma I_n^A - n\phi_A + P(A)$$

where the parameters have the same meaning as before, but refer to the species A. For convenience, it has been assumed here that both A and B ionize with the same charge ne in the field evaporation process.

Since the difference in the two activation energy values will decide which component will be preferentially field evaporating and to what extent, we determine $Q_A' - Q_B'$ to be

$$Q_A' - Q_B' = H_S + (\lambda_A^\circ - \lambda_B^\circ) + (\Sigma I_n^A - \Sigma I_n^B) + P(A) - P(B)$$

This expression is exact for field evaporation of A and B from the same or equivalent sites in the lattice. For atoms on different sites (sites that are on different planes or that have different coordination, etc.) the differences in binding energy and in the field enhancement factors operating at the two sites must be taken into consideration.

Brandon[18] has discussed in detail the case where the solute atoms, represented by β in our discussion, are preferentially evaporated. The field at any site is related to 1) the local radius of curvature, and 2) the local lattice geometry, usually, the lattice step height. For field evaporation on a high index plane, since the sublimation energies of atoms in the edges or at the interior differs only by the binding energy of the 3rd or 4th nearest neighbors, the activation energy for field evaporation is very nearly the same in the absence of any field enhancement. Of the field enhancement factors mentioned, the first one denoted by β_1 is not important for atoms on the same plane, thereby making the other factor β_2 to be responsible for edge atoms evaporating first. However, this factor drops off rapidly for lattice steps on crystal planes of increasing high index and it is therefore obvious that it is the magnitude of the difference $Q_A^i - Q_B^i$ which will decide if the solute atoms in the interior of the high index plane will also be field evaporated. If field evaporation takes place at lattice sites within a plane, then pitted surfaces are to be expected. As the differences get larger there will be random field evaporation from the low index planes as well. On the basis of such arguments, Brandon has predicted that the field ion images from a dilute alloy of a refractory metal in a less refractory matrix will be more regular than the image from the alloy of some components but with atomic fractions reversed.

4.4.2 Factors Affecting Field Evaporation in Alloys

Our discussion indicates that the greater the difference of $Q_A' - Q_B'$, the greater will be the difference in regularity of the micrographs from the end alloys. Before applying such a consideration to the Ta-Mo alloys, it is useful to consider the factors that determine the magnitude $Q_A' - Q_B'$. These are:

1) $\Delta\lambda$, the differences in sublimation energies of A and B,
2) ΔI, the differences in the ionization potentials of A and B,
3) polarization differences, P(A) - P(B), and
4) heat of solution.

Except of $\Delta\lambda$, all the other terms are only poorly known for the refractory metals, which are commonly studied with the field ion microscope. Still many useful qualitative conclusions can be drawn by considering them carefully. Since the calculated evaporation fields of pure metals do not include polarization corrections, the first two factors can be conveniently treated together and their effect will be indicated by the differences in the calculated evaporation fields Q_A and Q_B for these metals. These are listed in Table III.[18] If, on the other hand, the evaporation fields are determined by experiment, only heat of solution has to be considered separately. In the absence of such data, polarization differences have to be determined in an empirical manner as was described in the section on polarization effects. Either the compressibility data or the dimensionless parameter $(r_a - r_i)r_a^2$ which Brandon has employed[18] (r_a is half the nearest neighbor spacing and r_i is the univalent ionic radius) can be used as an index for the magnitude of polarization effect. The heats of solution, also, have to be similarly determined since thermodynamic data for these systems do not exist.

According to quasichemical theory, the heat of solution is positive if clustering occurs and negative if ordering is favored. Deviation from Vegard's law can give valuable information on short range ordering or clustering that is exhibited by an alloy. Thus, a positive deviation from Vegard's law can be identified with a tendency for clustering and, therefore, a positive heat of solution. Similarly, a negative deviation would imply a negative heat of solution.

4.4.3 Field Evaporation of Ta-Mo Alloys

These considerations can now be applied to the Ta-Mo system. The polarization effects of Ta and Mo have already been discussed and it was shown that P(Ta) - P(Mo) is expected to be considerable. Since, as Müller[11] has shown in the case of W, the polarization term will increase for the high index planes, ΔP for Ta-Mo alloys would also increase for such planes. The lattice parameter data of Fig.8(a) shows that there is a positive deviation in the Ta-end of the Ta-Mo phase diagram and thus a positive heat of solution is inferred. These two positive contributions along with the positive $\Delta Q (= Q_{Ta} - Q_{Mo}$, see Table III) will therefore make $Q^{*}_{Ta} - Q^{*}_{Mo}$ quite large. For this reason, it appears that the Ta-Mo micrographs are exceedingly disorganized in spite of the low solute content. It is also easy to see why this effect is not too pronounced in the W-Mo system. The compressibility data indicate that the polarization corrections should be approximately equal for W and Mo and the heat of solution from the lattice parameter data is inferred to be zero or negative. Thus $Q^{*}_{W} - Q^{*}_{Mo}$ is not large enough to cause serious irregularity in the W-Mo micrographs.

Table III Some useful properties of Mo, Ta and W.

Z	Element	ϕ (eV)	Λ (eV)	Q° (v/A)	$\Delta\gamma \cdot \gamma_a^2$ $\mathring{A}^3$	χ $cm^2/Kg \times 10^6$
42	Mo	4.30	6.15	3.8	0.74	0.36
73	Ta	6.15	8.25	4.6	0.96	0.48
74	W	4.52	8.67	5.7	0.77	0.31

ϕ work function

Λ sublimation energy

Q° evaporation field for evaporation as a doubly charged ion

χ compressibility

4.4.4 Extension to Other Systems

For any alloy system, Brandon's rule for the case of dilute alloys can be expected to hold true. The difference in the regularity of the two end alloys will be controlled by the difference $Q'_A - Q'_B$ and as seen above, this difference will be modified by both the polarization corrections and the deviation from randomness. Of the four refractory metals Nb, Ta, Mo, and W as shown in the section on polarization, Nb and Ta have high polarization corrections. If we associate short range ordering with a negative heat of solution and clustering with a positive heat of solution, - this is true for dilute alloys, - for the Nb-Mo, Nb W and Ta-Mo, TaW system the application of Vegard's law to the Nb and Ta ends indicate clustering and therefore a positive heat of solution. Since the polarization corrections also for the system will be large and positive, these alloys also will give irregular images at the Ta and Nb end. Mo-W and Nb-Ta on the other hand are expected to yield fairly regular images at both ends.

4.4.5 Field Evaporation from Concentrated Alloys

The case here is more complex because we encounter random evaporation from both solute and solvent atoms. In very simple terms the situation can be explained as follows: If the solute atom of a concentrated alloy is less easily evaporated the solute atoms left behind during field evaporation do not experience a field enhancement comparable to the case where the solute concentration is low and therefore tend to remain on the surface. It then follows that the concentration of the evaporating species will decide the extent of regularity of ion images. The situation is thus very different from the case of a dilute alloy and we can predict that a concentrated alloy of a refractory metal in a non-refractory matrix will show more irregularity than an alloy with the same components but with the atomic fractions reversed.

4.5 Image Contrast in Alloys

The field ion images from alloys are easily distinguished from those of a pure metal, from their gross irregularity. An exception is the case of the ordered alloy which, for all practical pruposes, behaves like a pure metal and develops very regular images. In general, the alloy micrographs do not develop high index planes, show the presence of dark or pitted regions where no imaging is probably taking place and a large number of bright spots which have been shown to arise out of polarization effects. It is clear that these effects are to be attributed to the field ionization and evaporation processes in the alloy and as we have already observed, these processes are modified to a considerable extent by the presence of the solute. The extent of this modification, though obviously dependent on the nature and concentration of solute, cannot still be predicted for a given system in our present state of understanding of image contrast in alloys.

4.5.1 A Single Criterion for Field Ionization and Field Evaporation Processes in Alloys

For understanding the contrast from alloys, we will, therefore, consider the effect of the field ionization and the field evaporation processes together as a single parameter. The strong resemblance of images, computed on the assumption that only atoms lying within a particular distance from the surface hemisphere can give rise to image spots to the actual field ion micrographs, indicates that such a consideration is useful. The irregularity of the alloy micrographs can then be attributed to the absence of a number of image spots. For convenience, we shall invoke a visibility criterion and then consider the characteristics of

the solute that could make the solute atom be totally invisible or either the solute or solvent atoms be partially invisible.

We have already discussed the factors that affect the field ionization process, namely the transfer of charge and size differences of the atomic constituents. The transfer of charge onto an atom results in the reduction of the local field and, hence, the ionization rate. The atoms may not then give rise to an image spot or the spot will appear dim. Similarly, the protruding atoms in an alloy, where the species have considerable size differences, will result in increased ionization over them with the result that the neighboring atoms may occur as weak spots. The appearance of polarization effects will accentuate this situation. A combination of these effects has been suggested to render the cobalt atoms in the ordered CoPt alloy,[19] invisible. Though the crystallography of the micrographs obtained from ordered CoPt are in accordance with the assumption that cobalt atoms are not imaged at all, it is hard to explain the absence of the superlattice planes consisting of cobalt atoms only, merely on the basis of field ionization effects. For these planes, where Co and Pt are distributed on alternate layers, charge spilling cannot be very important and it seems more attractive to consider the field evaporation effect to be more dominant. Because of the large differences in the evaporation fields of Pt and Co, the cobalt layers are possibly removed from the surface region of the specimen by field evaporation before imaging can take place. It is thus possible to treat the field ionization and evaporation phenomena together to explain the characteristics of alloy micrographs.

4.5.2 Computer Simulation

In order to check whether a single visibility criterion unifying

the field ionization and evaporation processes can lead to random surfaces characteristic of the alloy micrographs it was decided to run a computer program. It is now well realized that the general features of the field ion image of a pure metal can be explained in terms of the geometry of the approximately spherical surface which is obtained when a crystal lattice is cut by a sphere. Moore[20] was the first to point out that by assuming that only those atoms that lie within a shell of given thickness can give rise to spots, image patterns that strongly resemble the field ion images can be obtained with the help of a computer. Specifically the computer obtains the coordinates of the atoms within the shell. Recently Moore[21] has extended this work to solid solution alloys. To account for the different evaporative properties of the two species he assigned different shell thicknesses. A similar program has been performed on alloys of different compositions but with different criteria, which are described below.

4.5.2.1 Method of computation. Since the field ion images of the bcc metals Mo, Nb, W, and Ta generally correspond to a ⟨110⟩ wire texture, it was decided to obtain computed images corresponding to a ⟨110⟩ orientation. For this purpose the program developed by Ranganathan et al.[22] was suitably modified. In this method, a given crystal structure is considered in terms of the Bravais lattice. If the latter has centering then the structure can be generated by repeated application of the method to the primitive lattice with different coordinates for the origin. Since we are interested in the ⟨110⟩ orientation, we chose the coordinate axes to be [110], [1$\bar{1}$0] and [001]. With this set of axes, the bcc lattice becomes a face centered tetragonal lattice with a c/a ratio of 0.703

($= 1/\sqrt{2}$). It is therefore necessary to consider four primitive tetragonal lattices with origins at 000; $\frac{1}{2}\frac{1}{2}0$; $\frac{1}{2}0\frac{1}{2}$; and $0\frac{1}{2}\frac{1}{2}$. The crystal is projected onto the (110) planes and the radii R_A and R_B of the circles obtained by the intersection of the spherical shell with the {110} planes are determined (Fig. 22). The distances of all the atoms on the basal plane from the origin are calculated and compared with the different sets of (R_A R_B) values. The coordinates of an atom are recorded only if it falls within any set of these values. Since the stereographic projection is a nearer approximation to the field ion image, the orthographic coordinates were first converted to the stereographic ones and the Cal-Comp plotter subroutine was used to plot the simulated image. The computations were programmed in FORTRAN for Control Data 6600 Computer. Figure 23 gives the computed image for a bcc metal of radius 200a where a is the lattice parameter.

4.5.3 Random Alloys

The above program corresponds to the case of a pure metal. First the random alloys were considered. For the application of the visibility criterion, according to which the solute atoms are totally invisible, a control statement was introduced that permitted the coordinate of an atom to be recorded only if the random number generation function exceeded the solvent content of the alloy. This allows for a random distribution of the two species with the solute atoms not participating in the image.

Figures 24 (a-e) show the computed images for bcc lattice with compositions of 90%, 80%, 70%, 60% and 50% of solvent. A 10% interval was chosen to detect any onset of irregularity clearly. The computed images correspond to a radius of 200a and the value of P, the shell thickness,

was chosen to be 0.05a. Moore and Ranganathan[23] have used a similar value for a fcc lattice of comparable radius. There is very little difference in Figs. 24 (a-c) in terms of the regularity, size, and number of planes. Only the number of points have decreased which is not easily distinguished by the naked eye. The computed images from 60% and 50% solvent alloys are somewhat irregular. A comparison of these images with those obtained from the Ta-Mo system or the W-Mo system clearly indicate the field ion patterns from alloys are considerably more irregular than the computed images. A count of the spots from the micrographs of the Ta-Mo alloys with 10% and 50% solute contents does not indicate a sharp reduction in the number of spots. Further, since it is only the appearance of a few rows of atoms in any plane that makes the plane recognizable, it follows that the onset of irregularity is a critical function of the radius and that for the same alloy there will be improvement in regularity with increase in radius. Prolonged field evaporation of the Ta-Mo alloys resulting in considerable change of the radius was not observed to have any marked improvements of the regularity of ion images. A similar observation has been made by Brenner[11] on the regularity of Pt-10Ir alloy micrographs during prolonged field evaporation. It is to be concluded that the total invisibility criterion is too great an oversimplification to yield computed images comparable to the observed alloy micrographs. It is proposed to consider cases where solute and solvent atoms follow some type of partial visibility criterion. A useful start can be to assume that a solute atom will be invisible if it is surrounded by more than a fixed number of solvent neighbors.

4.5.4 Clustered Alloys

So far, a random distribution has been assumed for the atomic species of the alloy. When deviations from such randomness exist, the contrast to be expected will be, in general, partly due to the intrinsic imaging behavior of the species, modified by the presence of the second component, and partly due to the interface effect. An interface can be defined to separate regions of a crystal different in structure and/or composition. While the interface effect is, therefore, not important for a random distribution or short range ordering, it should have marked influence in the case of clustering, since a clustered situation necessarily implies regions of different composition. The interface effect, however, will be confined to the interface only.

The simplest case of an interface will be a high angle boundary. Since alloy micrographs are strongly irregular, high angle grain boundaries are difficult to be observed and analyzed. Other types of interfaces are 1) an intermediate phase, and 2) a precipitate or a Guinier-Preston zone. The σ-phase in W-34 Re[3] has been shown to give enhanced contrast near the interface with a high degree of bright spots and in spite of the lack of crystalline regularity of the disordered matrix, a partial coherency was inferred from the continuity of atomic planes along the interface. Similarly a NiBe-Ni solid solution interface has been reported by McClane and Müller.[24] The intermediate phase has a CsCl structure while the solid solution has a fcc structure. A second interface across which complete coherency was observed has been identified as a G.P. zone. Müller[17] has also reported the observation of a lens shaped martensite plate in a high carbon steel. It must be

conceded that all these identifications are still tentative, since no characteristic crystal planes of the second phase have been observed in the micrographs.

To understand the type of contrast that can be expected from clustered alloys, computations were performed with a specific model of clustering. A model, whereby the composition varied in a sinusoidal manner radially along the crystal, was assumed in order to minimize computational difficulties. The radial distribution ensured that there is no crystallographic habit for the clustering present.

For this clustering case, the parameters that can be varied are the period and amplitude of the sinusoidal variations of the composition. The mean composition was held at 50-50 and the clustering period was assumed to be fifteen (110) planes (= $15 \frac{a}{\sqrt{2}}$ Å where a is the lattice parameter). To introduce this clustering model, the distance of an atom that lays within any annulus from the apex was calculated and converted into $2R\Pi + \theta$ radians by dividing by 2Π/period. Then $\alpha \cos\theta + 0.5$, where α is the clustering amplitude, is the solvent concentration on the spherical surface with radius corresponding to the distance of the atom under consideration from the apex (Fig. 25). Now the visibility consideration is applied by the control statement that allows the recording of the atom coordinates only if the random generating function exceeded $\alpha \cos\theta + 0.5$. This was repeated for all atoms in any annulus.

Figures 26 (a-d) show the computed images from a 50-50 alloy with a clustering distribution. The period is a constant $15a/\sqrt{2}$Å for all cases and the amplitudes vary from 0.1 to 0.4 in steps of 0.1. It is seen that the computed images for small deviations are as irregular as those from random alloys of the same composition. When the deviations increase to

0.3 and 0.4 a band structure becomes marked. The regions with fewer spots, obviously, correspond to the regions where solute atoms are concentrated. Though the weakness of the total invisibility criterion becomes again readily apparent, the interface effect offers some insight as to the nature of micrographs obtainable from clustered alloys. It is seen that the band structure becomes marked only if the deviations from the random composition are substantial and also if the width of the clustered zone is small in comparison to the radius of the tip. When clustered regions have a larger width, it is obvious that the interface effect can be missed.

4.5.5 Demixed Alloys

A case where clustering width exceeds such limits is that of a demixed alloy. In this situation it is not possible to detect the demixing effects from a single micrograph.

An interesting case of demixing has been reported in Ta-Mo alloys in the high concentration range.[7] Segregation of the two species here occurs with a crystallographic habit. In the Mo-rich alloys this composition deviation is on a {200} plane and in the Ta-rich alloys the deviations occur on {110} planes. The result of such demixing is the formation of domains richer in either of the two components of the alloy than warranted by the nominal composition. We have already mentioned that though Ta and Mo are bcc metals of the transition type their ion images display distinct singularities. Each has an image of typical but different intensity distribution. Also Ta develops {200} planes very well while Mo does not. Thus on crossing from a Ta-rich region to a Mo-rich region the image characteristics should change in a marked fashion.

Experimentally, pulsed field evaporation was performed on a number of Ta-50Mo tips. About 200 micrographs covering a distance of about 800Å were

obtained in a single field evaporation sequence and were analyzed for effects mentioned above. Except for local clustering effects, evidence for demixing was not detected. This could very well mean that the width of demixed zones is larger than 1000Å.

4.6 Distinguishing Between Atomic Species

The above discussion leads to the important question of whether absolute identification of the two species on the micrographs is possible. The question is still a largely unanswered one. The problem is of considerable interest because a method to identify the two species will give a clear picture about the field ionization and evaporation processes and also about the surface distribution of atoms. The latter information can be used, with the help of field evaporation, to shed light on the extent of local ordering present in the alloy. Curiously enough an indirect method for distinguishing between atomic species has been developed for a case when the distribution of atoms, however, is precisely known. For instance, in the case of ordered equiatomic Co-Pt alloy, the observed field ion images agree with computed structures if the assumption that one kind of species is not imaged. It was previously mentioned that if the local field strength and therefore the field ionization rate above an atom is drastically reduced, the atom does not give rise to an image spot. In Pt-Co the invisible species has been identified to be Co atoms and the reduction in field strength has been attributed to the size effect, a charge smoothing effect of the Smoluchowski type or a valence effect, the latter two resulting in a spilling of electronic charge from the Pt atom to the Co atom. Similarly the micrographs obtained from ordered Ni_4Mo[25] correspond very well with lattice structure obtained from the Mo sites only.

In particular cases, large brightly emitting image points away from the normal zone lines have been associated with impurity atoms such as carbon, oxygen and nitrogen. Thus oxygen matrix concentration in iridium has been calculated by Fortes and Ralph[26] from the number of bright spots. While the authors attribute the brightness of spots corresponding to such impurity atoms to a fairly large and less localized perturbation due to these atoms, it seems more likely as mentioned before that the brightness associated with these gas molecules originates from the increased binding energy by field penetration polarization, as a result of which the critical distance for ionization, x_c, is reduced.

The situation with disordered alloys, however, is complex. The field ionization and evaporation processes from alloys are not clearly understood and until such time a general theory for identification of species seems unlikely. A method for identification of species due to Ralph and Brandon,[27] has been found to be very subjective. It is based on the voltage analysis of the number of image points. The graph of the number of points against the applied voltage was shown to possess a linear relationship for a pure metal but a discontinuity was observed in the case of an alloy. The discontinuity was found to be proportional in magnitude to the solute content in W-Re alloys. The application of this method to the Ta-Mo alloy system did not show a linear relation as well as any discontinuity. A similar conclusion has been reached by Brenner from his work on Pt alloys.[11]

We have already mentioned the possibility of using specific effects of the solute atoms, to obtain useful though qualitative information about the distribution of the two species. For instance, Ta unlike Mo or W is known to develop the {200} planes and their vicinities to a very high

perfection. An examination of the regularity of the {200} planes in a Ta-Mo alloy will thus give information on the Mo content in those planes, since a decrease in the Mo content is expected to result in a better developed {200} plane and an increase in a more random {200} plane. The variation of such regularity over continued field evaporation will thus indicate a variation of the Mo content. Figure 21, mentioned earlier, was interpreted to show clustering on this basis. Similarly the resolution in the {222} regions of the Mo-based alloys can be interpreted to show the relative concentration of the solute atoms in any evaporation sequence.

During the pulsed field evaporation of the Ta-Mo alloys an alternative possibility to distinguish between the Ta and Mo atoms was observed. All the Mo-8Ta micrographs, as mentioned before, show a small number of bright spots in the usually less intense region between {110} and (200) planes and a small number of weak spots in the intense triangle region. The Ta atoms on the other hand are expected to be bright in the first region and weak in the second. This leads to the possibility that there could be a one-to-one correspondence between such spots and Ta atoms. It is, on this basis, that in the evaporation sequences, Figs. 16 and 17, the atomic identification of the groups of atoms that evaporated, has been made. This method receives further support from the discussion on polarization effects in alloys, since bright spots occurring in the region of {110} to {200} even if attributed to the polarization effects, would be identified as due to Ta atoms.

4.7 Summary of the Results

The main objectives of this research, to recapitulate, have been twofold: the first being to increase the state of knowledge on the field ion microscopy of alloys with particular emphasis on how the solute affects the field ionization and field evaporation of the matrix atoms, and the second it to categorize the segregation effects that become important enough at high concentration levels to make the alloys brittle.

The first objective has been met satisfactorily. Alloy micrographs representative of a complete system have been obtained so that comparisons can be made with available data on other systems. The factors affecting field ionization and evaporation have been discussed so that micrographs from other alloys can be studied on a firmer basis. Computer simulation work has also been shown to be useful in understanding the nature of alloy micrographs.

As for the second objective the results obtained are still inconclusive. It has been mentioned earlier, that the brittle nature of the concentrated Ta-Mo alloy emanate from the size differences of the two atomic species which result in the clustering of the two components on specific crystallographic planes. Since the elastic compliances of the two metals are expected to determine what these crystal planes will be, a consideration of these properties of Ta and Mo becomes important. The ion images of Ta and Mo are characteristically different from each other and these differences have been enumerated earlier.

Since Ta and Mo also exhibit dissimilar elastic anisotropies, it seems logical to consider that the elastic anisotropy of metals can play an important role in the field ionization process. A similar suggestion that the nature and the number of bonds in specific crystallographic

regions on the specimen surface may be as important as polarization effects in determining the nature of ion images, has been voiced by Knor and Müller[28] in the 14th Field Emission Symposium. However a deeper understanding of the field ionization process is essential to carry this suggestion to a more precise form.

The evidence on clustering is however is quite strong. Field evaporation experiments show the width of the demixed zones suggested by Van Torne and Thomas[7] to be the cause for embrittlement, must exceed 1000Å, though clear evidence for their existence has not been obtained. However the tendency for clustering in regions less than 50Å in width has been established and this clustering situation has been observed on the {200} planes. This result is in accordance with earlier suggestions[6] made on the basis of compliance data that such deviations from random distributions would occur on {200} planes.

It is now proposed to perform a more detailed electron microscopy investigation in an attempt to determine the size of the demixed regions, using dark field and split Kikuchi line techniques. The alloy Ta-44Mo that is expected to be most demixed[7] should be particularly suited for this work.

5. CONCLUSIONS

1. A field ion microscope study of the tantalum-molybdenum system has been carried out at liquid hydrogen temperature and micrographs have been obtained from Ta, Ta-10 a/o Mo, Ta-50 a/o Mo, Mo-8 a/o Ta and Mo.

2. The Ta-Mo alloy micrographs obtained show far more irregularity than those from W-Mo alloys. As in the W-Mo system there is an asymmetry of the regularity about the 50% solute here also but the sense of asymmetry is opposite. It is the Mo-end alloy which is more regular than the Ta-end alloy.

3. Physical and electronic factors have been shown to affect the nature of alloy micrographs. Thus the Mo-8Ta micrographs show much less distortion in the {222} region than pure Mo and the Ta-50 Mo alloy micrographs resemble those of W-alloys with uniform intensity distribution.

4. The bright spots obtained in these alloy micrographs have been attributed to size differences in the atomic species which result in surface protrusions. The increased local field as well as field penetration polarization both increase the ionization rate over such protruding atoms resulting in bright spots.

5. The greater regularity of Mo-8Ta micrographs over those from Ta-10 Mo has been shown to be in accord with predictions based on field evaporation from dilute alloys but the unexpected large difference in the regularity has been explained by accounting for the polarization and heat of solution terms in the field evaporation equation.

6. A single visibility criterion for both the field ionization and field evaporation processes, has been proposed. The far too regular computed images from random and clustered alloys that have been obtained

on the assumption that solute atoms do not participate in the imaging show that a total invisibility criterion is an oversimplification. A band structure has been shown to result when the deviation from randomness is appreciable in the clustered alloys.

7. Evidence for local clustering has been obtained from pulsed field evaporation of the Ta-50 Mo alloy. The study of a large number of micrographs obtained in this fashion did not reveal the contrast effects that have been predicted for a demixed alloy of the Ta-Mo system. It has been concluded that the width of the demixed zones exceed 1000Å.

ACKNOWLEDGEMENTS

The author would like to express his deep gratitude to Prof. Gareth Thomas for his guidance and encouragement throughout the course of this research. He is indebted to Dr. Srinivasa Ranganathan for the help in the construction of the field ion microscope and for the many valuable discussions. Thanks are also due to the Technical Photography Section for their excellent support.

This research was carried out under the auspices of the United States Atomic Energy Commission through the Inorganic Materials Research Division of the Lawrence Radiation Laboratory, Berkeley, California.

REFERENCES

1. J. M. Sivertsen and M. E. Nicholson, Prog. Mat. Sci. 9, 305 (1961).
2. E. K. Caspary and E. Krautz, Z. Naturforsch. 19a, 591 (1964).
3. B. Ralph and D. G. Brandon, Phil. Mag. 8, 919 (1963).
4. W. DuBroff and E. S. Machlin, Proc. 13th Field Emission Symposium, Cornell University, Ithaca, New York, 1966.
5. L. I. Van Torne, (Ph. D. Thesis) University of California, Berkeley, UCRL-11752, Jan. 1965.
6. R. Gomer, Field Emission and Field Ionization (Oxford University Press, London, 1961).
7. L. I. Van Torne and G. Thomas, Acta Met. 14, 621 (1966).
8. S. Nakamura and E. W. Müller, J. Appl. Phys. 36, 2535 (1965).
9. E. W. Müller, J. Appl. Phys. 37, 4346 (1966).
10. M. Semchyshen and R. Q. Barr, Arc-Cast Molybdenum-Base Alloys, Summary Report NR039-002, 1955.
11. S. S. Brenner, Short Course on Field Ion Microscopy, University of Florida, 1966.
12. S. Ranganathan, J. Appl. Phys. 37, 4346 (1966).
13. E. W. Müller, Science 149, 6591 (1965).
14. T. T. Tsong and E. W. Müller, J. Appl. Phys. 37, 3065 (1966).
15. E. W. Müller, Surface Science 2, 484 (1964).
16. D. G. Brandon, Phil. Mag. 14, 803 (1966).
17. E. W. Müller, et al., J. Appl. Phys. 36, 2496 (1965).
18. D. G. Brandon, Surface Science, 3, 1 (1965).
19. T. T. Tsong and E. W. Müller, J. Appl. Phys. 38, 545 (1967).

20. A. J. W. Moore, 11th Field Emission Symposium, Cambridge University (unpublished) 1964.

21. A. J. W. Moore, Phil. Mag. (in press).

22. S. Ranganathan, H. R. Lyon and G. Thomas, J. Appl. Phys. (in press).

23. A. J. Moore and S. Ranganathan, submitted to Phil. Mag.

24. S. B. McLane and E. W. Müller, 12th Field Emission Symposium, Pennsylvania State University, 1965.

25. R. W. Newman, B. G. LeFevre and J. J. Hren, 13th Field Emission Symposium, Cornell University, Ithaca, New York, 1966.

26. M. A. Fortes and B. Ralph, Acta Met. 15, 707 (1967).

27. B. Ralph and D. G. Brandon, J. Roy. Mic. Soc. 82, 179 (1964).

28. Z. Knor and E. W. Müller, 14th Field Emission Symposium, Washington, D. C. (unpublished).

APPENDIX 1

DETERMINATION OF THE SIGN OF THE BURGERS VECTOR FROM FIELD ION MICROGRAPHS

The determination of the Burgers vector of dislocations in field ion specimens has been dwelt upon in Sec. 3.4. Here the relation of the nature of the spiral contrast (right-handed or left-handed) to the sign of the Burgers vector is discussed.

The sign of the Burgers vector, $\vec{b}$, of any dislocation is a quantity beset by much arbitrariness. It is dependent on the line sense $\vec{\ell}$ and on the coordinate system if the line sense is considered part of it; on the nature of the Burgers circuit, i.e., whether it is right-handed or left-handed, sighting down on the dislocation in the "positive" direction and whether the closure feature is expressed as the finish-to-start or the start-to-finish vector. The effect of all of these arbitrary conventions is to make the Burgers vector point in either of the two directions and hence, only two notations need be considered to make the sign of the Burgers vector unambiguous. In Burgers notation, the Burgers circuit is defined in the imperfect crystal in a clockwise fashion while looking at a dislocation in the positive direction and the finish-to-start vector is the Burgers vector. In Frank's notation, the circuit is made in the perfect crystal and hence the opposite sign is obtained. We shall adopt the Burgers definition. The Burgers notation is illustrated in Fig. 27 (a).

As mentioned in Sec. 3.3, the information concerning the Burgers vector to be gained by observation in the field ion microscope is given by the scalar product:

$$(\vec{g} \cdot \vec{b}) = n$$

$\vec{g}$ being the vector normal to the plane of observation. It is obvious that n represents the projection of $\vec{b}$ perpendicular to the planes in units of $d = \frac{1}{(g)}$. Its sign is positive or negative depending upon whether the projection of $\vec{b}$ points in the direction of $\vec{g}$ or opposite to it.

Since $\vec{b}$ and therefore n can have either sign unless the line sense is fixed, we make the further assumption that the positive direction of the dislocation is the one as it emerges from the crystal. In the Burgers notation which is being used, depending upon whether $\vec{\ell} \cdot \vec{b}$ is positive or negative a left-handed or right-handed spiral results.

In the field ion microscope, the image seen by the camera corresponds to looking at the specimen from the tip side and the image is recorded in the positive print in the same relation. Therefore a right-handed circuit (clockwise looking at the positive direction) around thd dislocation with $\vec{\ell} \uparrow\uparrow \vec{b}$ gives an anticlockwise spiral in the print; if $\vec{\ell} \uparrow\downarrow \vec{b}$ a clockwise spiral results. The second case is illustrated in Fig. 27 (b). In field ion images, it is therefore evident that a clockwise spiral implies that $\vec{g} \cdot \vec{b}$ is negative and an anticlockwise spiral that it is positive.

In favorable cases, a single micrograph can be used to determine the sign of the Burgers vector. For instance, let us consider an a/2 ⟨111⟩ dislocation line in a plane labelled (321) in the field ion micrograph of a bcc metal. Since $\vec{g} \cdot \vec{b}$ is different for each of the four possible Burgers vectors a/2[111], a/2[$\bar{1}$11], a/2[1$\bar{1}$1], and a/2[11$\bar{1}$], the number of spirals will uniquely determine the Burgers vector to be one of the four or its opposite vector. The sense of the spiral can now be used to decide on either of the two. A three-leaved right-handed spiral or (321) can

to be interpreted to indicate a dislocation with the Burgers vector to be a/2 $[\bar{1}\bar{1}\bar{1}]$. Since Fig. 18 shows a two-leaved left-landed spiral on the (130) plane the Burgers vector can be either a/2[111] or a/2$[11\bar{1}]$.

The line sense $\vec{l}$ can be determined by field evaporation when the nature of the dislocation can be completely determined. Sign $(\vec{l} \cdot \vec{b})$ will decide the nature of the screw component, left-handed if positive, right-handed if negative, and $\vec{b} \times \vec{l}$ will decide the position of the extra plane.

The author would like to thank Dr. S. Ranganathan for valuable discussions on this section.

APPENDIX 2

CONTRAST FROM DISLOCATION LOOPS

In ideal cases, the contrast from dislocation loops can be simply obtained by superposition of the effects of the two line segments of the loop intersecting the surface. In practice, the identification of a loop can become complicated if the loop intersects the specimen at two different net planes or at more than two points. We shall discuss here the simple case of a dislocation loop intersecting a single crystallographic plane at two points (Fig. 28 (a)).

The nature of the contrast can be directly used to determine whether the loop is perfect or faulted. If the atomic rings join up elsewhere except at the extra half plane the loop is a perfect one. A discontinuity on one side of which the rings are shifted with respect to those on the other indicates a faulted loop. However if $\vec{g} \cdot \vec{b} = 0$ when $\vec{b}$ is the Burgers vector of the loop, no contrast due to the loop will be observed and it is not possible to differentiate between a faulted and a perfect loop. Since stacking faults in bcc metals are not well understood, only perfect loop contrast is described here.

The contrast due to the loop in Fig. 28 (a) will be the sum of the separate effects due to the line segments. Since the dislocation has different line sense at these points, the sense of the spirals will be opposite and Fig. 28 (b) illustrates the cumulative effect assuming that a single spiral is formed at each point. It is seen that an extra (or incomplete) ring results. In general, if the Burgers vector of the dislocation is such that an n-leaved spiral results at an intersection, n incomplete rings will result as a result of the dislocation loop cutting the surface at two points.

Determination of the Burgers Vector of the Loop

It is customary to define the Burger circuit around a dislocation loop such that the Burgers vectors of all segments of the loop are identical. This results in the assigning of opposite line senses to the dislocation loop as it emerges at two points on the crystal.

However, since the contrast in the field ion image is the cumulative effect of two separate dislocation lines, the assumption that the positive direction of the line is the one that as it emerges from the crystal will result in giving opposite Burgers vectors to the two segments. The sense of the spiral of the intersection points will enable the assigning of the proper Burgers vector at these points. Thus if Fig. 28 (b) is assumed to be a contrast of a loop intersecting the (321) plane on a bcc metal, the single spiral will imply the Burgers vector to be $a/2[1\bar{1}1]$ or $a/2[\bar{1}1\bar{1}]$. Since at point A the spiral is anticlockwise the Burgers vector at A is $a/2[1\bar{1}1]$ and the Burgers vector at B is therefore $a/2[\bar{1}1\bar{1}]$.

Determination of the Nature of the Loop

The nature of the loop, i.e., whether it is of the vacancy or interstitial type, can be easily determined if the loop plane is known. If $\vec{\ell}_A$ and $\vec{\ell}_B$ at points A and B can be determined and if $\vec{\ell}_A$ is not parallel to $\vec{\ell}_B$ the cross product $\vec{\ell}_A \times \vec{\ell}_B$ or $\vec{\ell}_B \times \vec{\ell}_A$ will define the loop plane. If $\vec{\ell}_A$ and $\vec{\ell}_B$ are parallel, field evaporation of a known number of atomic rings coupled to a simple geometric construction can be employed to determine the loop plane. If $\vec{b}_A$ and $\vec{b}_B$ are the Burgers vectors corresponding to $\vec{\ell}_A$ and $\vec{\ell}_B$ then $\vec{\eta}_A = \vec{b}_A \times \vec{\ell}_A$ are $\vec{\eta}_B = \vec{b}_B \times \vec{\ell}_B$ will define the extra half planes for the two segments of dislocation. It is clear that if the extra planes are outside the loop, the loop is of vacancy type. If the extra planes are inside, the loop is interstitial in origin.

FIGURE CAPTIONS

Fig. 1 Schematic view of the field ion microscope.

Fig. 2 Image formation in FIM (from Müller).[11]

Fig. 3 Schematic view of the hydrogen liquifier.

Fig. 4 Schematic View of the FIM unit.

Fig. 4(a) Legend for Fig. 4.

Fig. 5 Photograph of the FIM unit.

Fig. 6 Microscope head and the liquifier.

Fig. 7 Schematic view of the pulse generator.

Fig. 8 (a,b) a) Lattice parameter and b) mechanical property data for the Ta-Mo alloy system (from Van Torne and Thomas),[7] present data in (a).

Fig. 9 Ta-Mo phase diagram.

Fig. 10 Helium ion micrograph of Ta at 77°K.

Fig. 11 Helium ion micrograph of Ta at 21°K.

Fig. 12 Helium ion micrograph of Mo at 21°K.

Fig. 13 Helium ion micrograph of Mo-8Ta at 21°K.

Fig. 14(a) Helium ion image of Mo-8Ta at 77°K (imaging voltage 9kV).

(b) Same specimen after considerable field evaporation.

(c) Same at best imaging voltage (imaging voltage 10 kV).

Fig. 15 Mo-8Ta micrograph at 21°K showing good resolution and little distortion in the {222} region.

Figs. 16 (a,b) and 17(a,b) Pulse evaporation sequence showing the evaporation of a group of atoms tentatively identified as Mo and Ta respectively. In both cases (b) was obtained by a single pulse of height 1 kV and width 30μs.

Fig. 18 Mo-8Ta micrograph showing dislocation contrast at region marked A.

Fig. 19 (a,b) Helium ion micrograph of Ta-10Mo at 21°K showing great irregularity (c) and the presence of bright spots (b).

Fig. 20 Helium ion image of Ta-50Mo at 21°K.

Fig. 21 (a-c) Ta-50Mo micrographs showing a tendency for clustering in the {200} regions.

Fig. 22 Tip geometry for computation.

Fig. 23 Computed patterns for a project bcc crystal in the (110) orientation. Radius = 200a shell thickness = 0.05a.

Fig. 24 (a-e) Computed patterns with total invisibility of solute atoms from alloys of 90, 80, 70, 60, and 50% solvent content.

Fig. 25 Cluster geometry for computation.

Fig. 26 (a-d) Computed patterns for clustered alloys (with the clustered model of text). Average composition 50% solvent. Cluster period $15a\sqrt{2}$ Å and amplitudes 0.1, 0.2, 0.3, and 0.4, respectively.

Fig. 27(a) Burgers notation for the Burgers vector.

(b) Spiral contrast in FIM image.

Fig. 28(a) Dislocation loop and specimen geometry.

(b) Dislocation loop contrast.

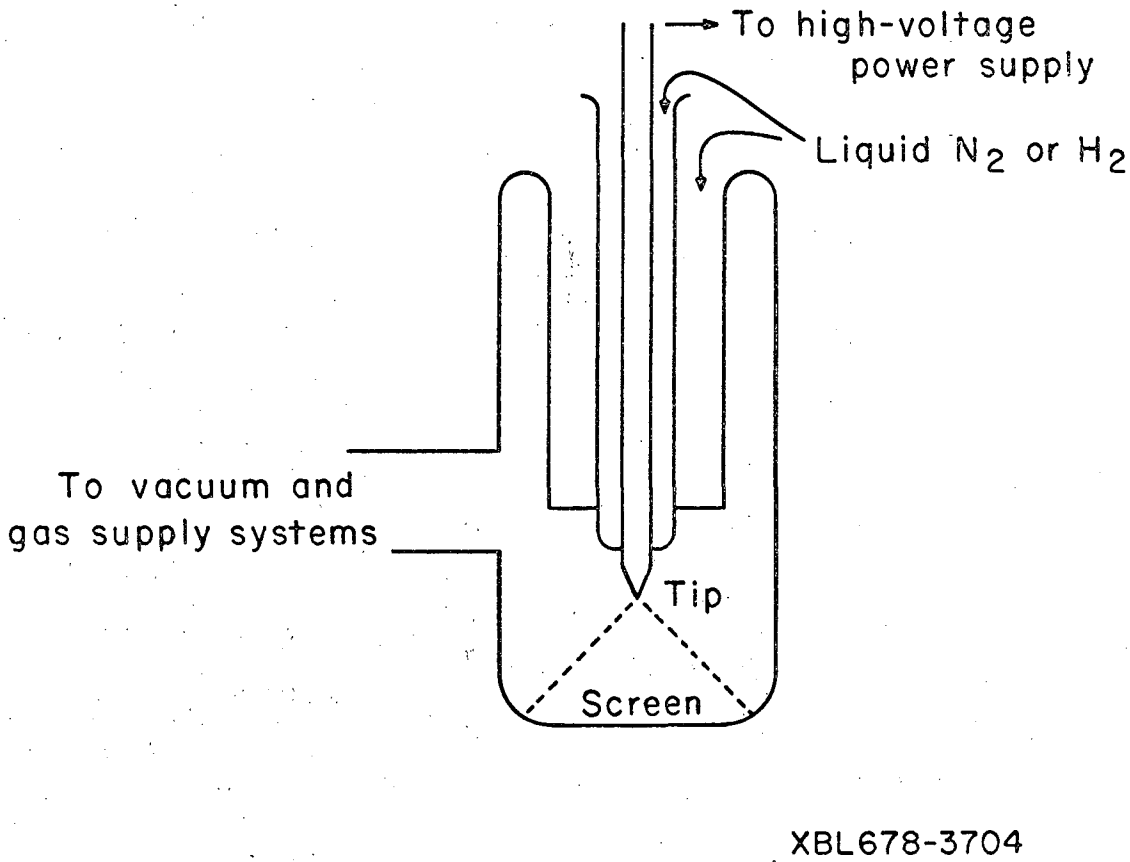
To high-voltage
power supply
Liquid N_2 or H_2
To vacuum and
gas supply systems
Tip
Screen
XBL678-3704

Fig. 1

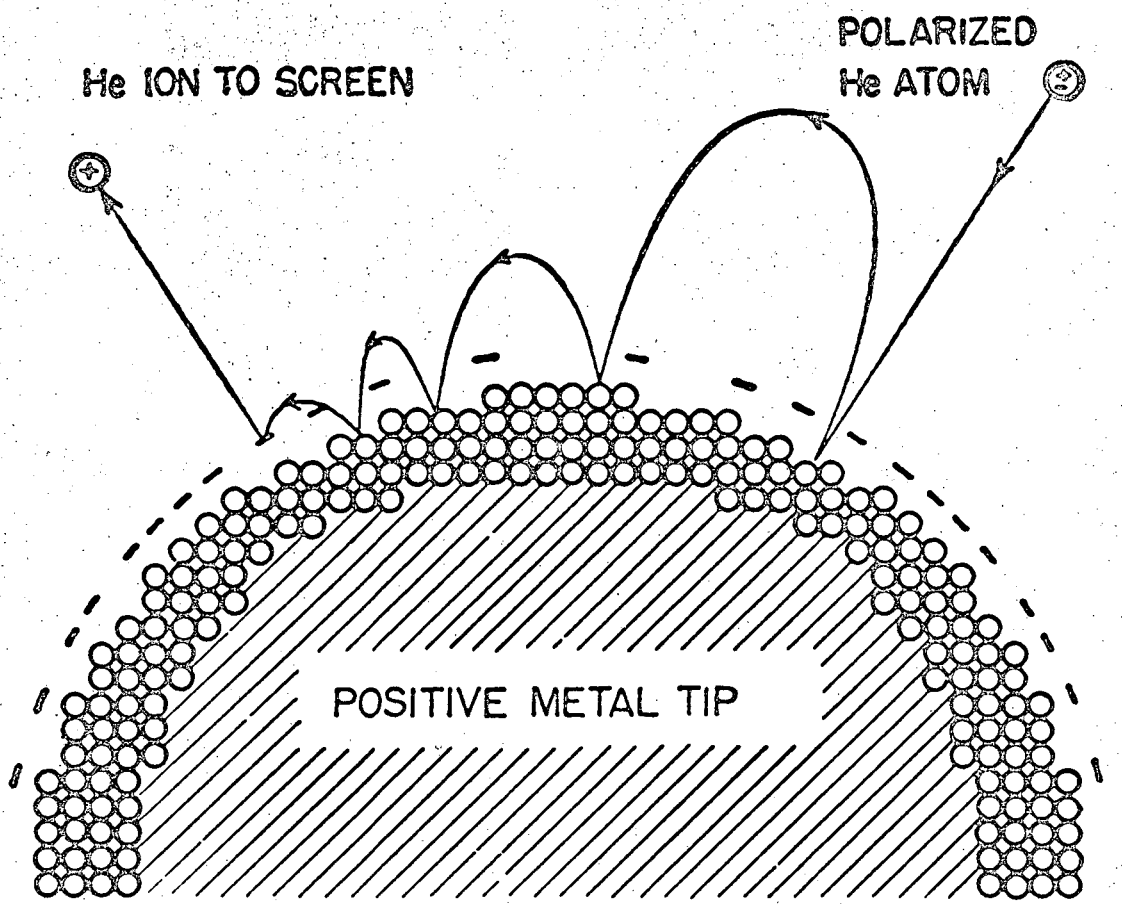

XBL 678-4464

Fig. 2

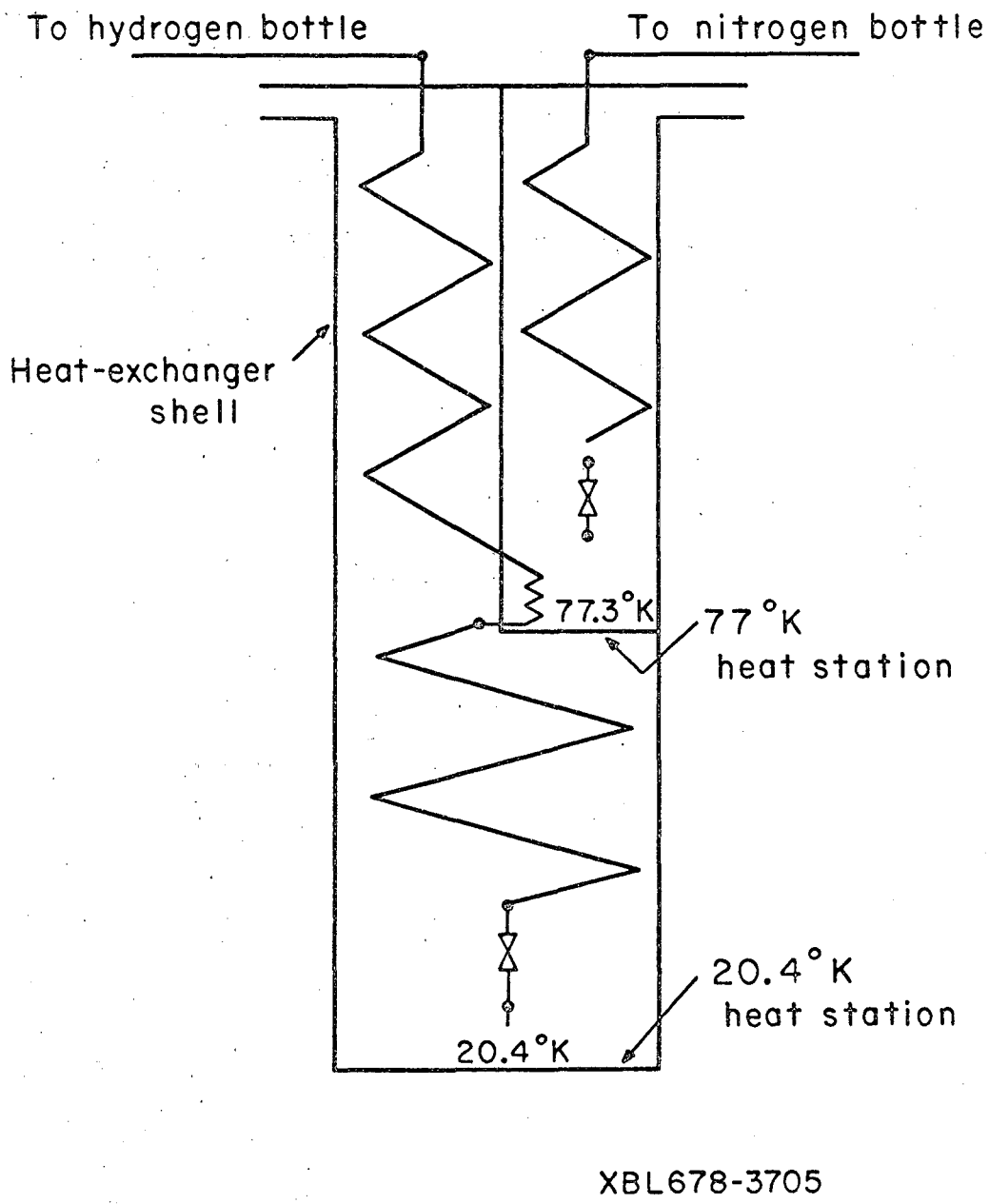
To hydrogen bottle
To nitrogen bottle
Heat-exchanger shell
77.3°K
77 °K heat station
20.4°K
20.4 °K heat station
XBL678-3705

Fig. 3

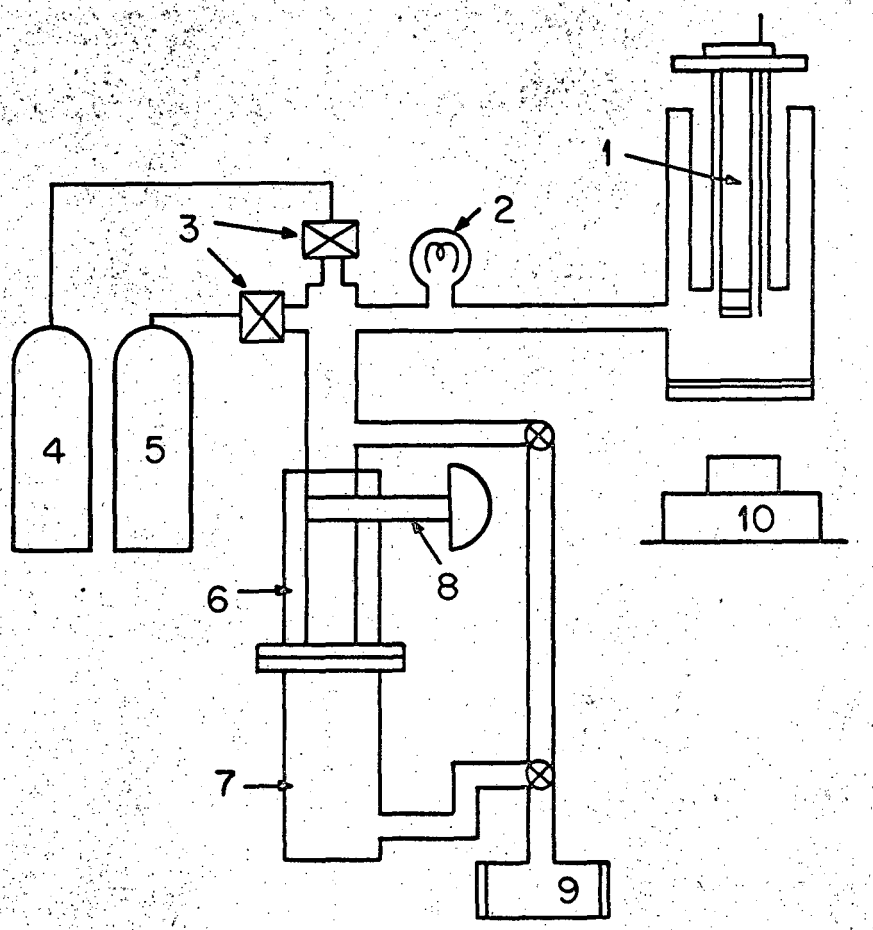

XBL678-3706

Fig. 4

(For legend see following page)

LEGEND FOR FIG. 4

1. Microscope head with cryotip
2. Ionization gauge
3. Leak valves for imaging gases
4. Research grade helium
5. Research grade hydrogen or neon
6. Liquid nitrogen trap
7. Diffusion pump
8. High vacuum valve
9. Roughing pump
10. Camera

XBB 676-3495

Fig. 5

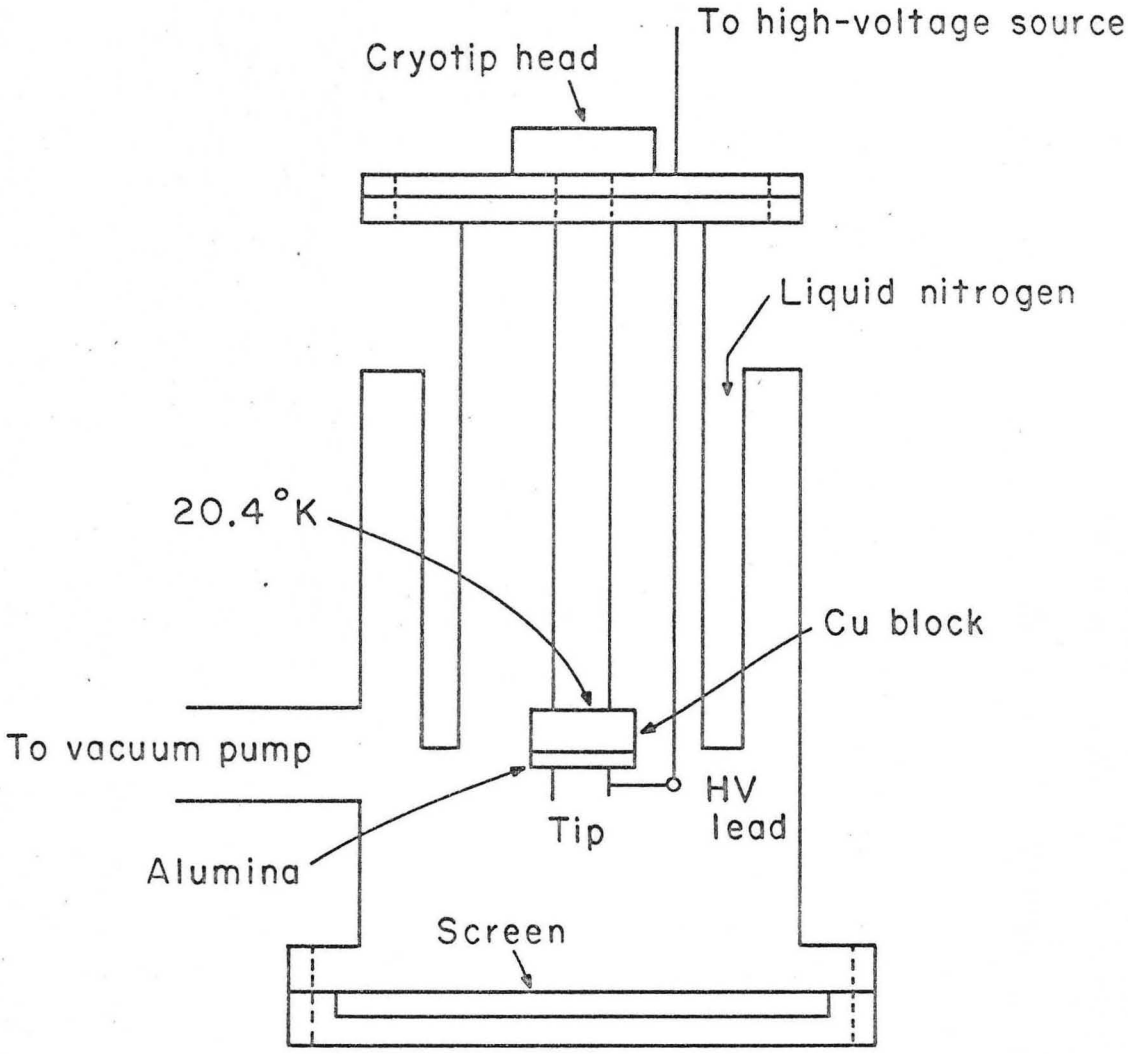

XBL678-3707

Fig. 6

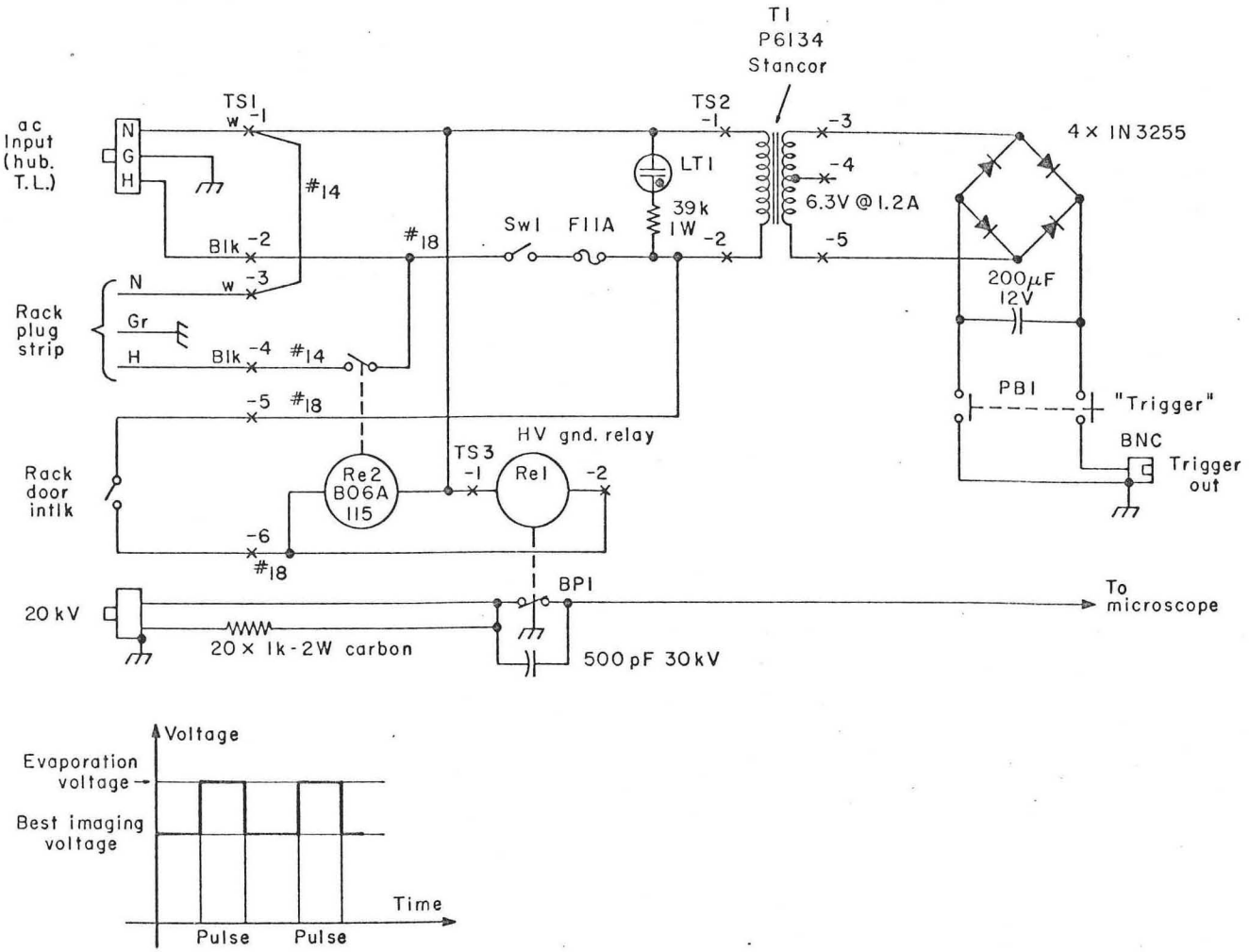

XBL676-3356

Fig. 7

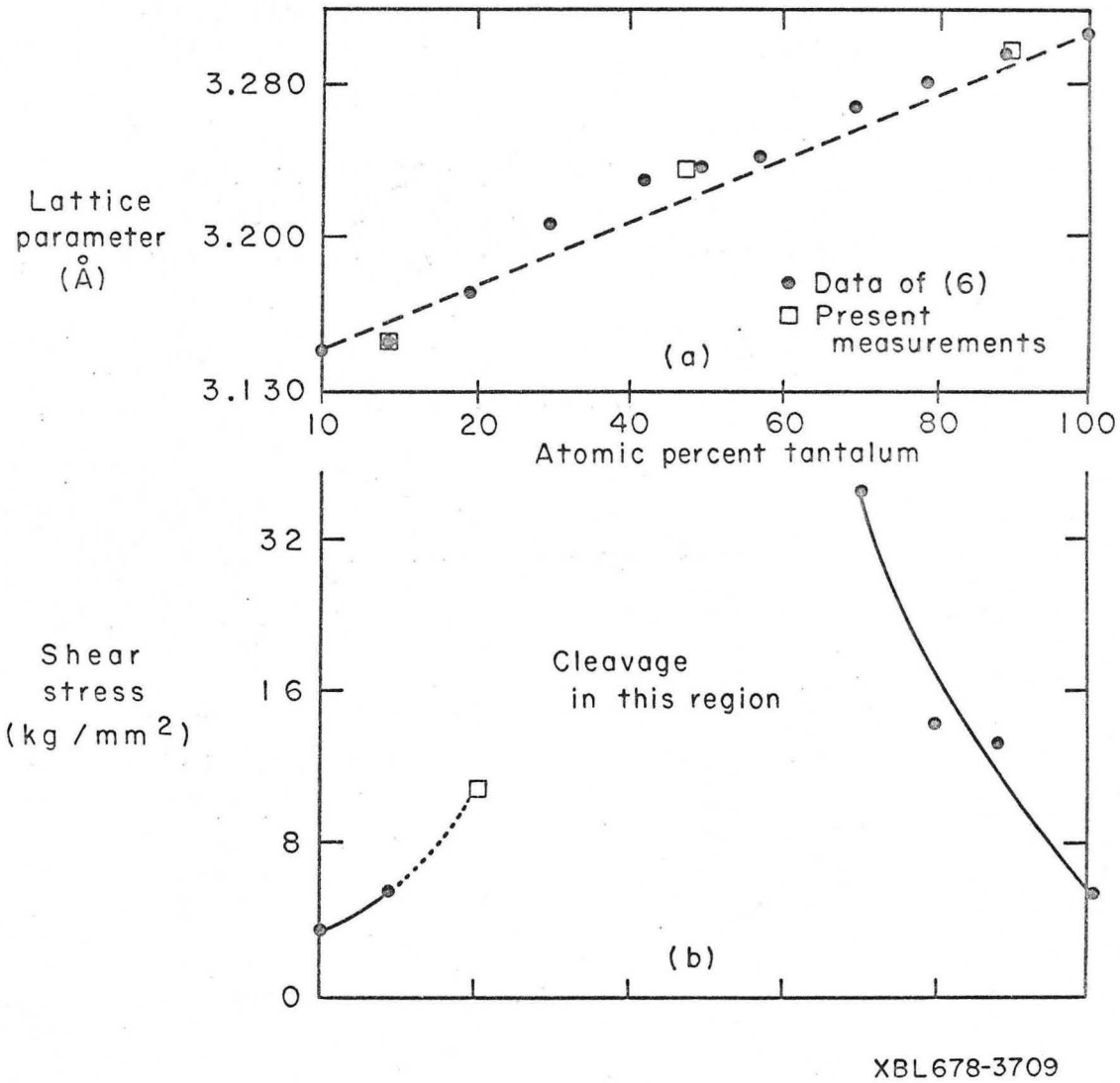

XBL678-3709

Fig. 8

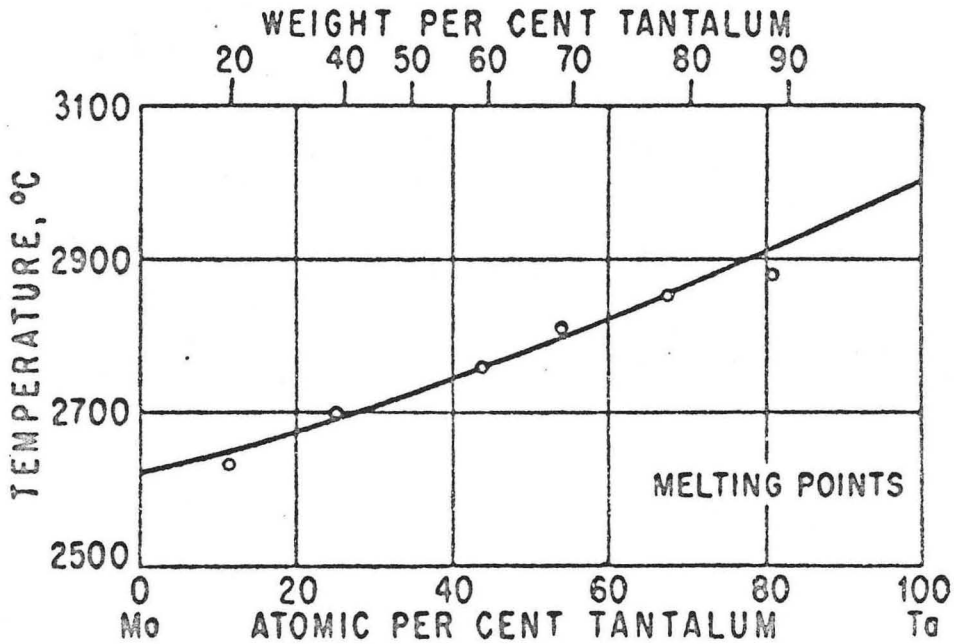

XBL 678-4465

Fig. 9

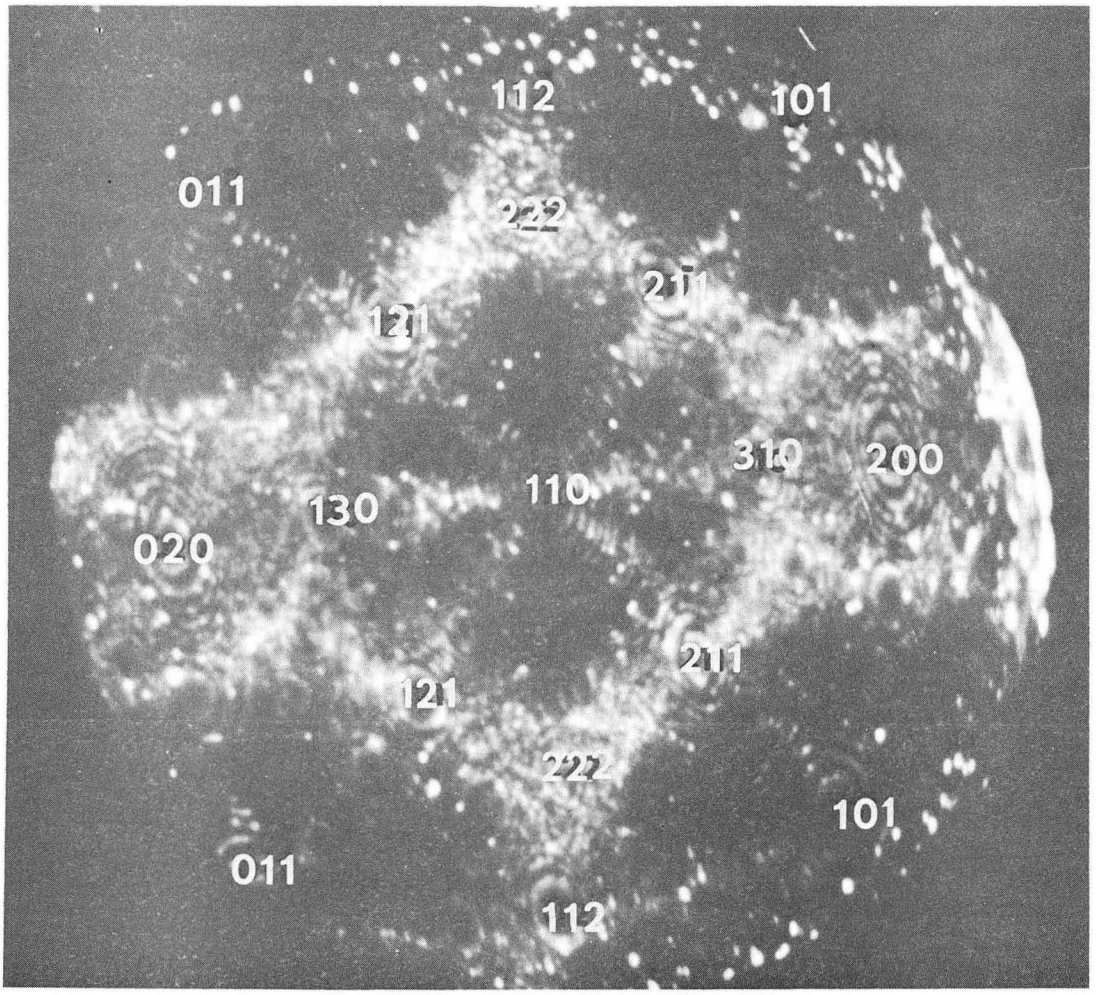

XBB 678-4455

Fig. 10

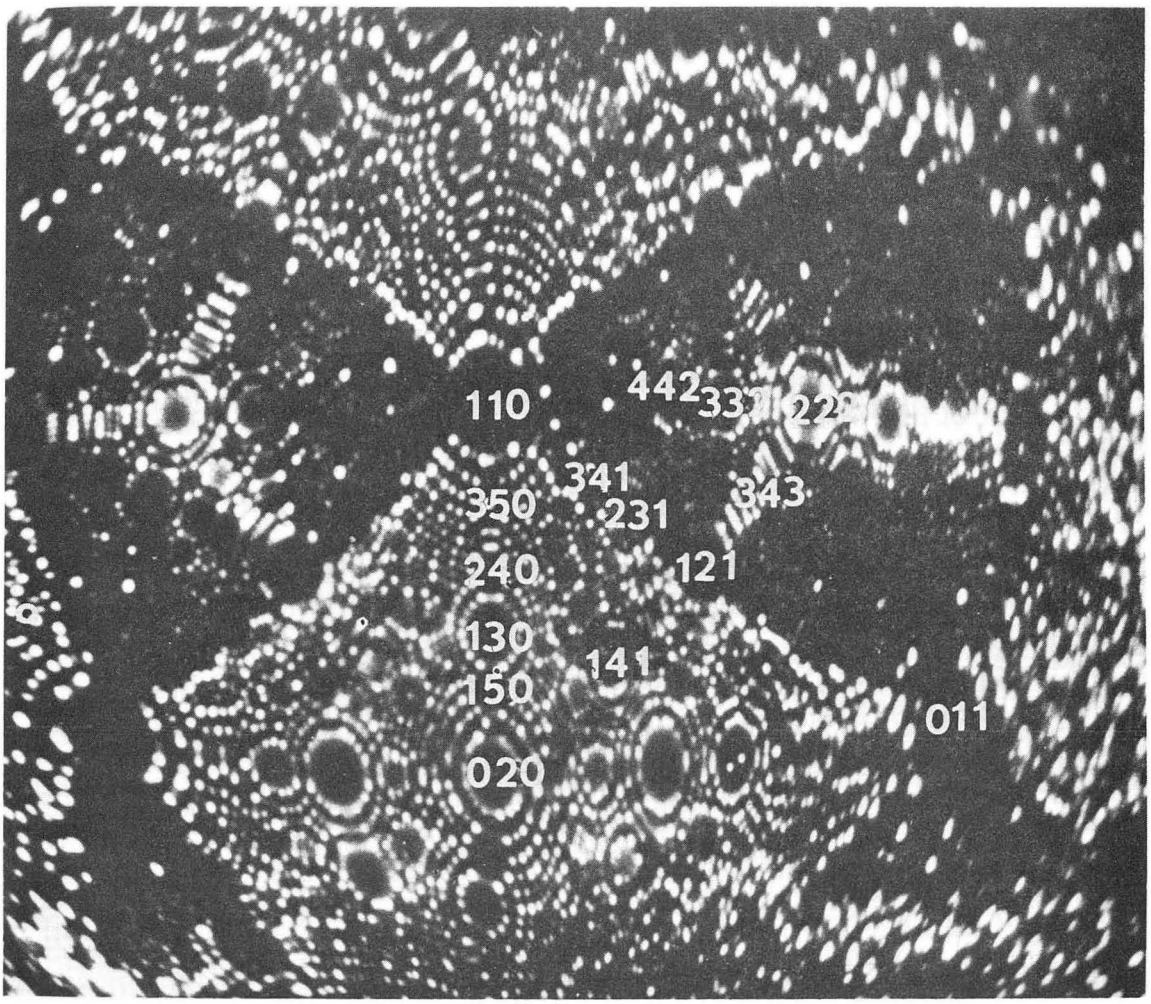

XBB 678-4452

Fig. 11

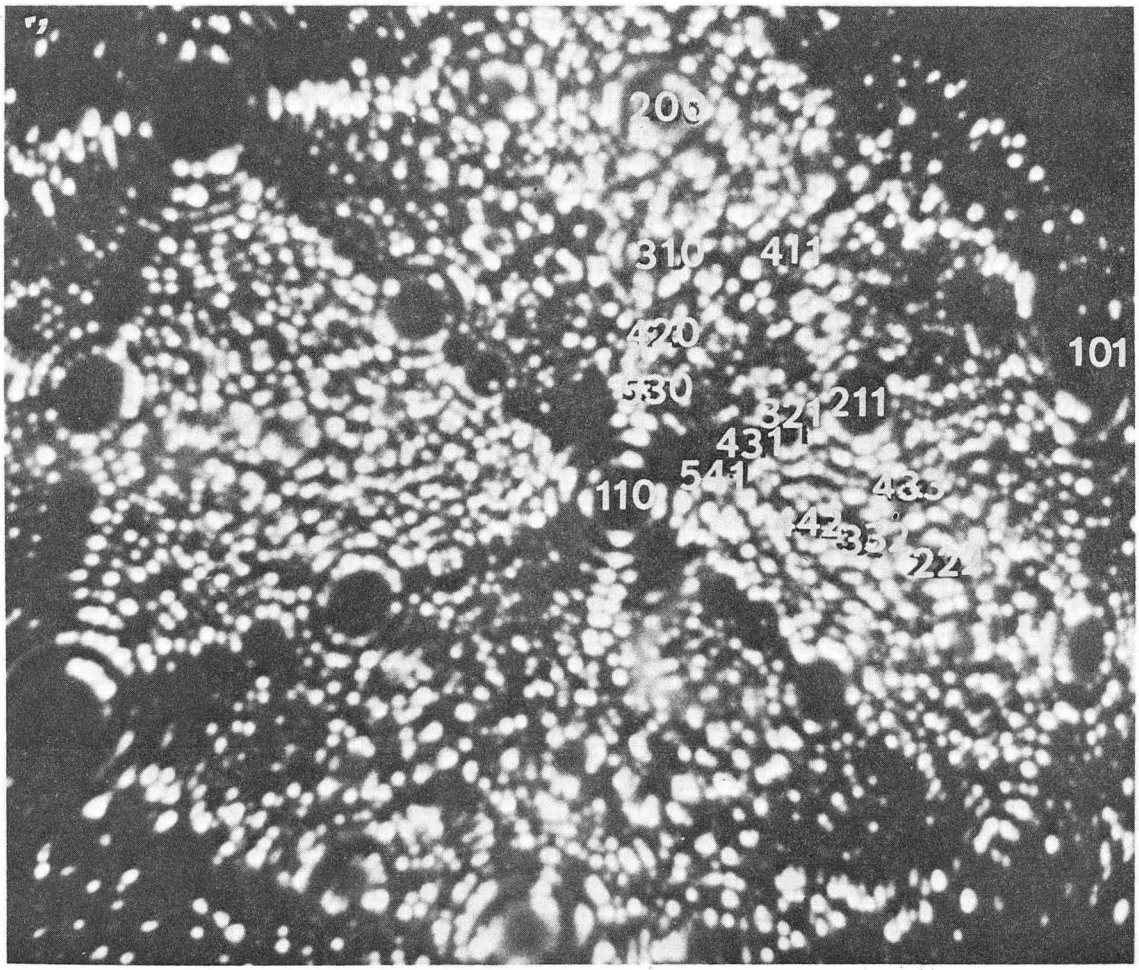

XBB 678-4453

Fig. 12

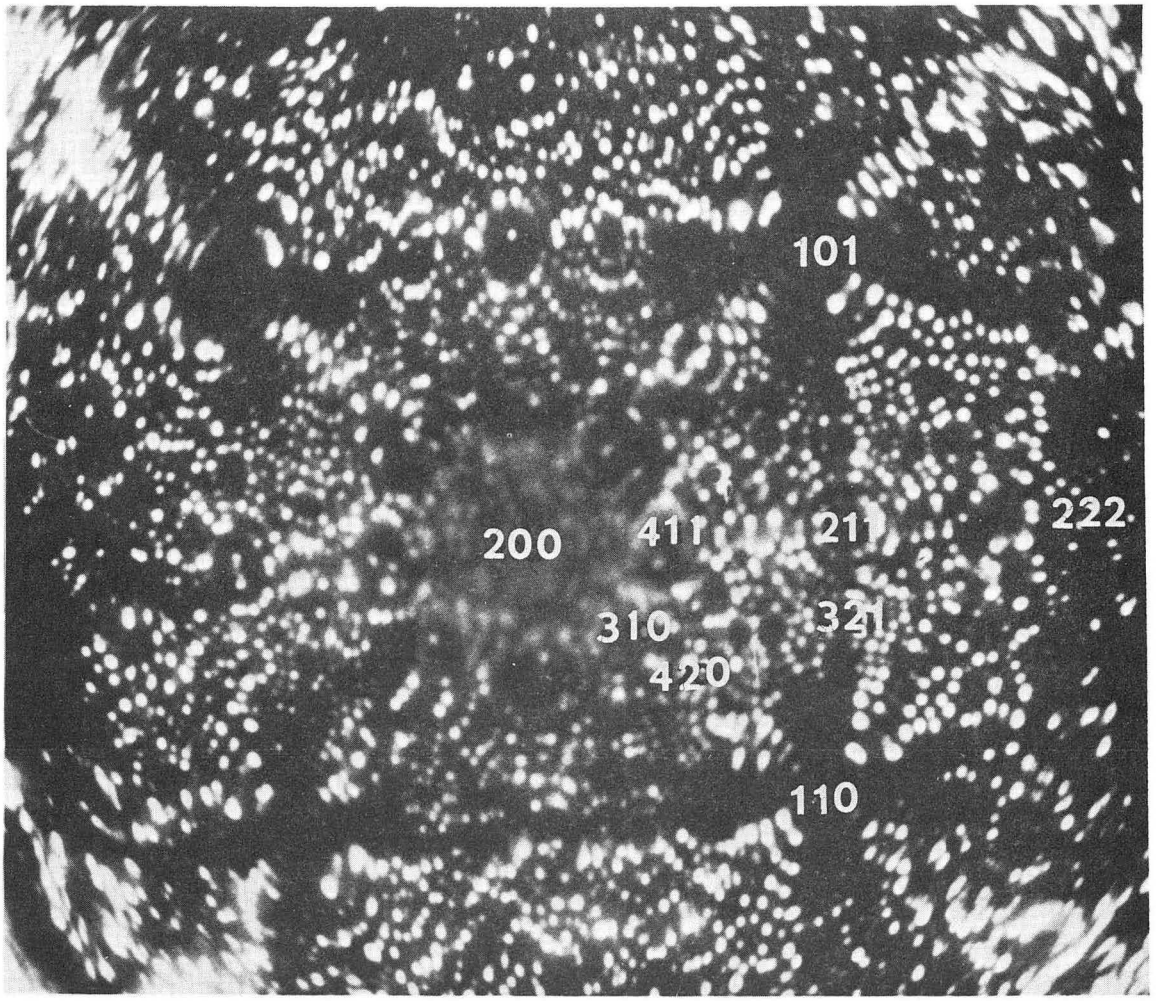

XBB 678-4454

Fig. 13

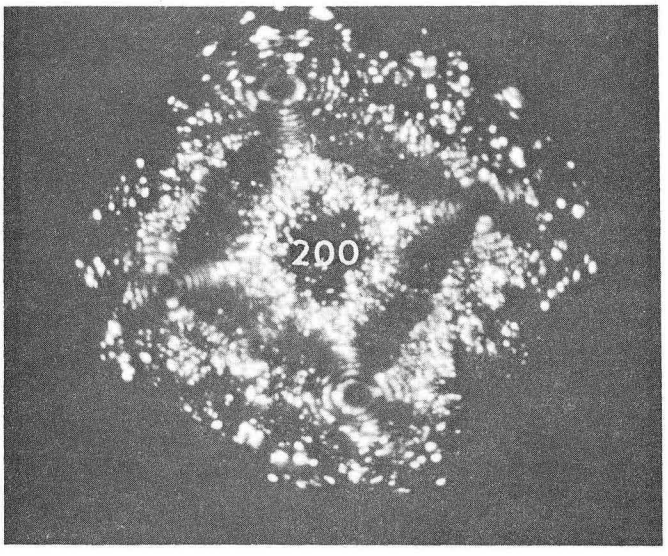

Fig. 14 (a)

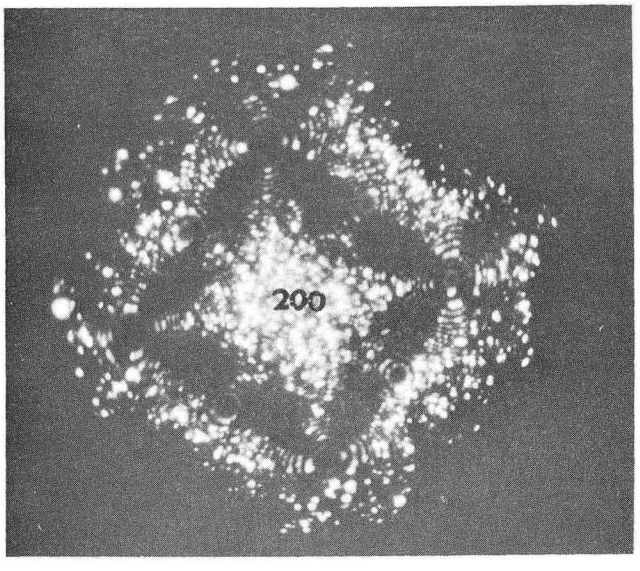

XBB 678-4456

Fig. 14 (b)

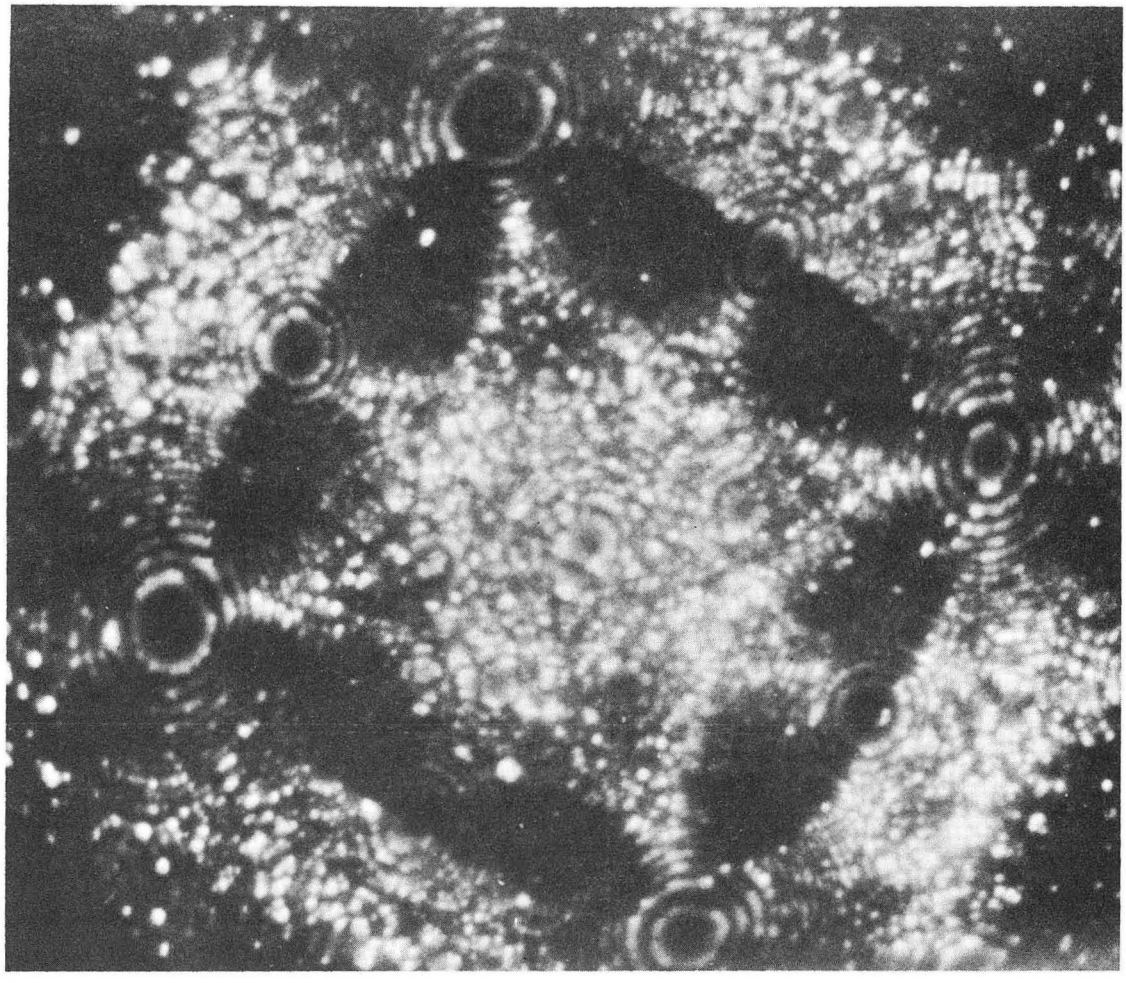

XBB 678-4451

Fig. 14 (c)

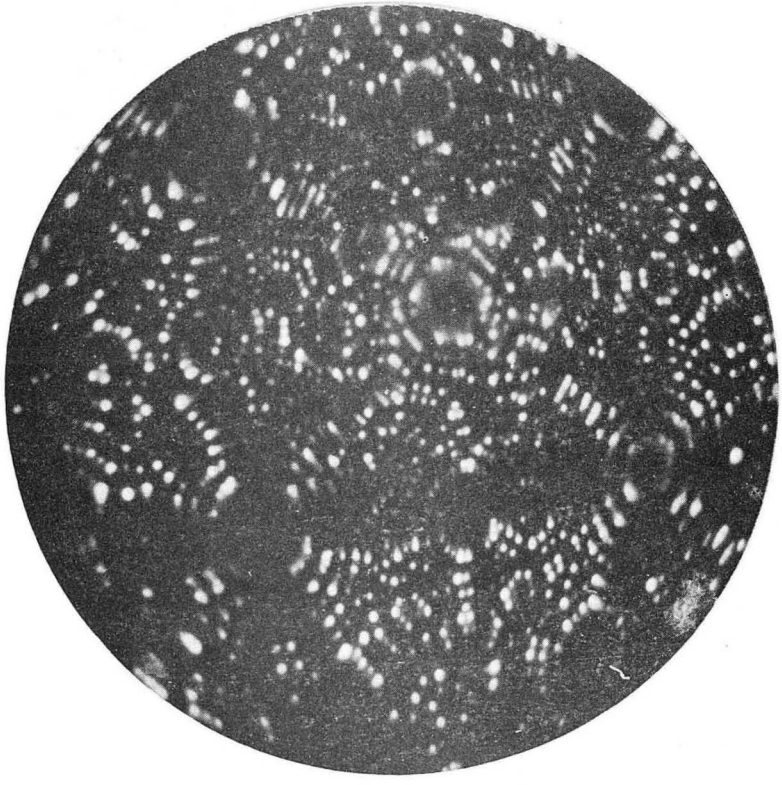

XBB 678-4462

Fig. 15

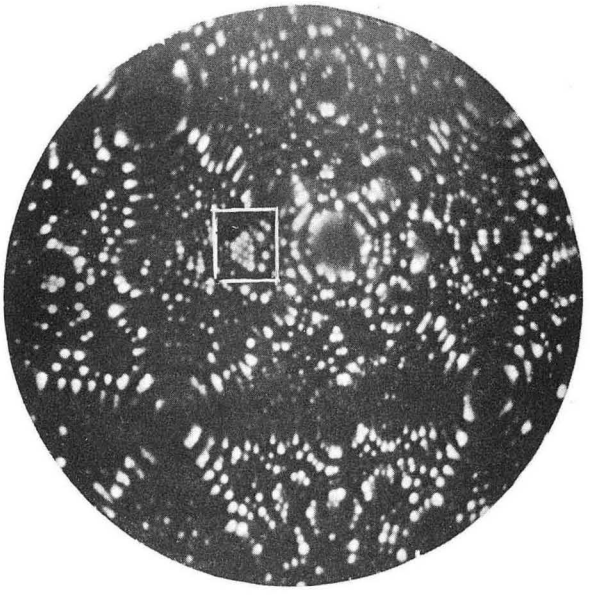

Fig. 16 (a)

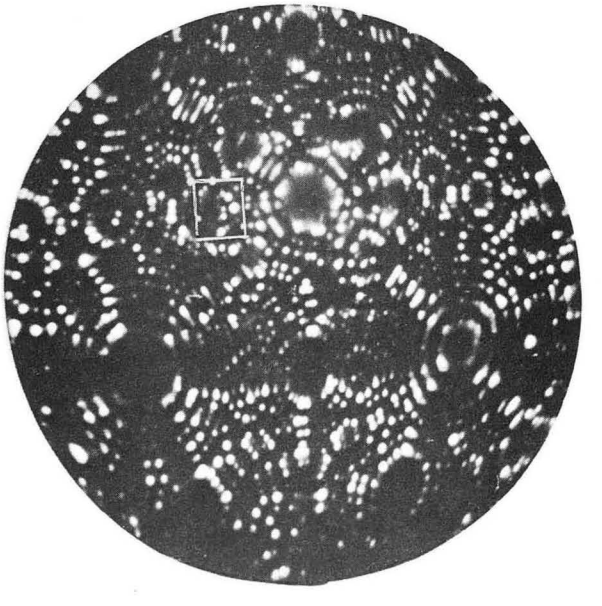

XBB 678-4450

Fig. 16 (b)

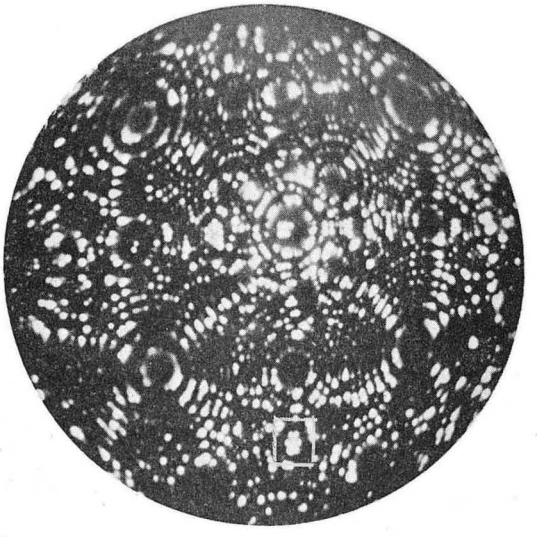

Fig. 17 (a)

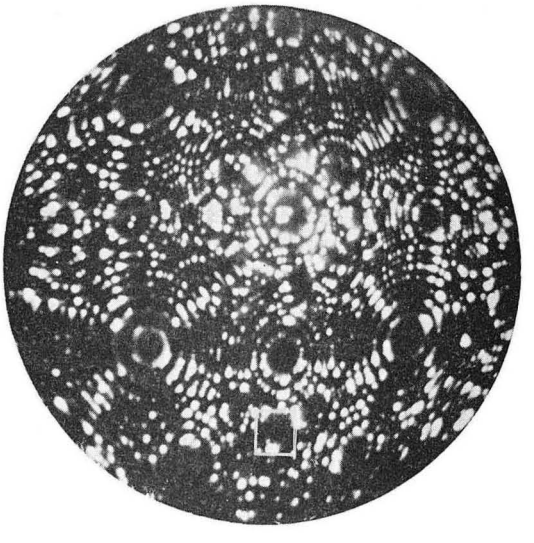

XBB 678-4460

Fig. 17 (b)

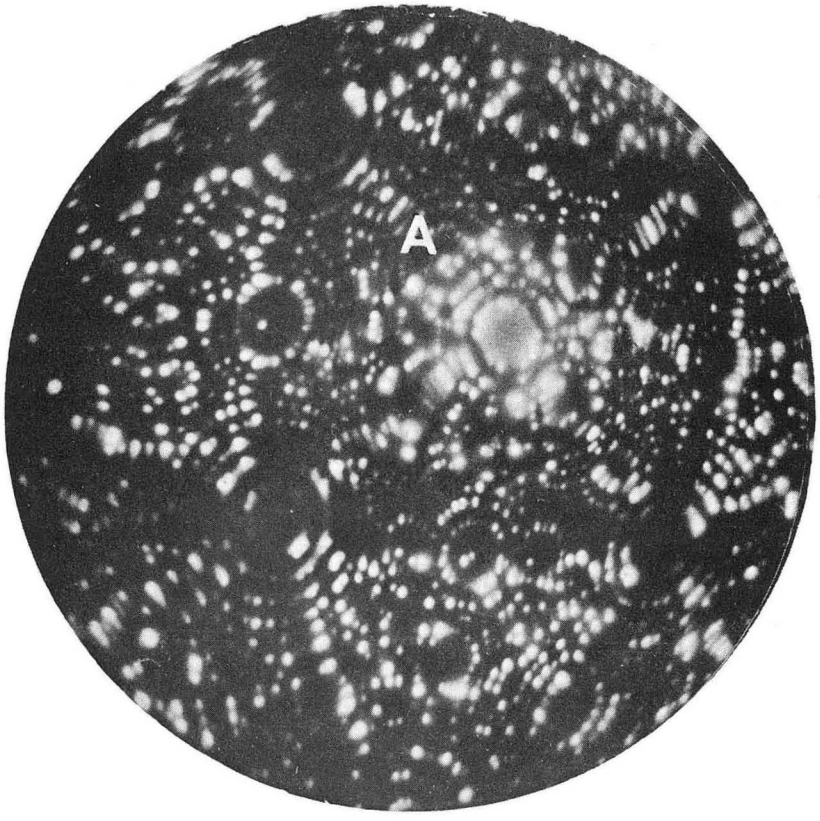

XBB 678-4461

Fig. 18

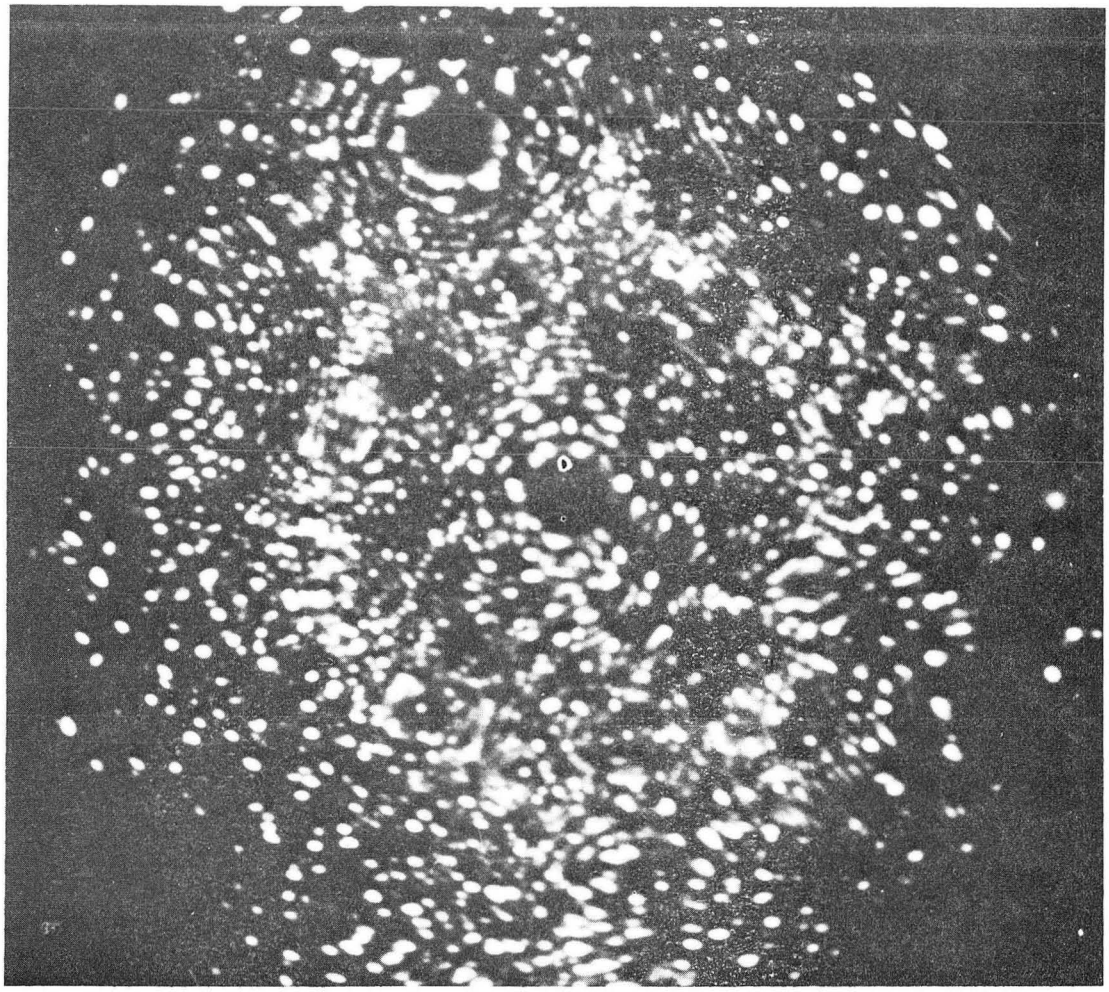

XBB 678-4458

Fig. 19 (a)

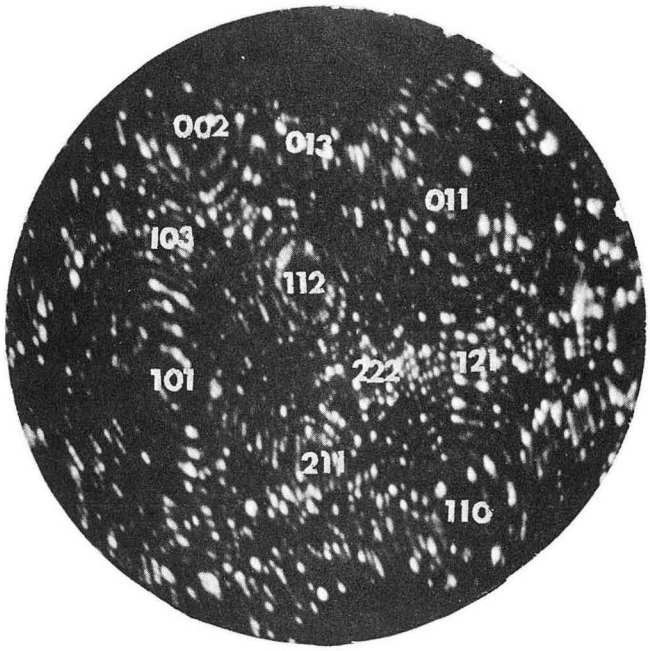

XBB 678-4457

Fig. 19 (b)

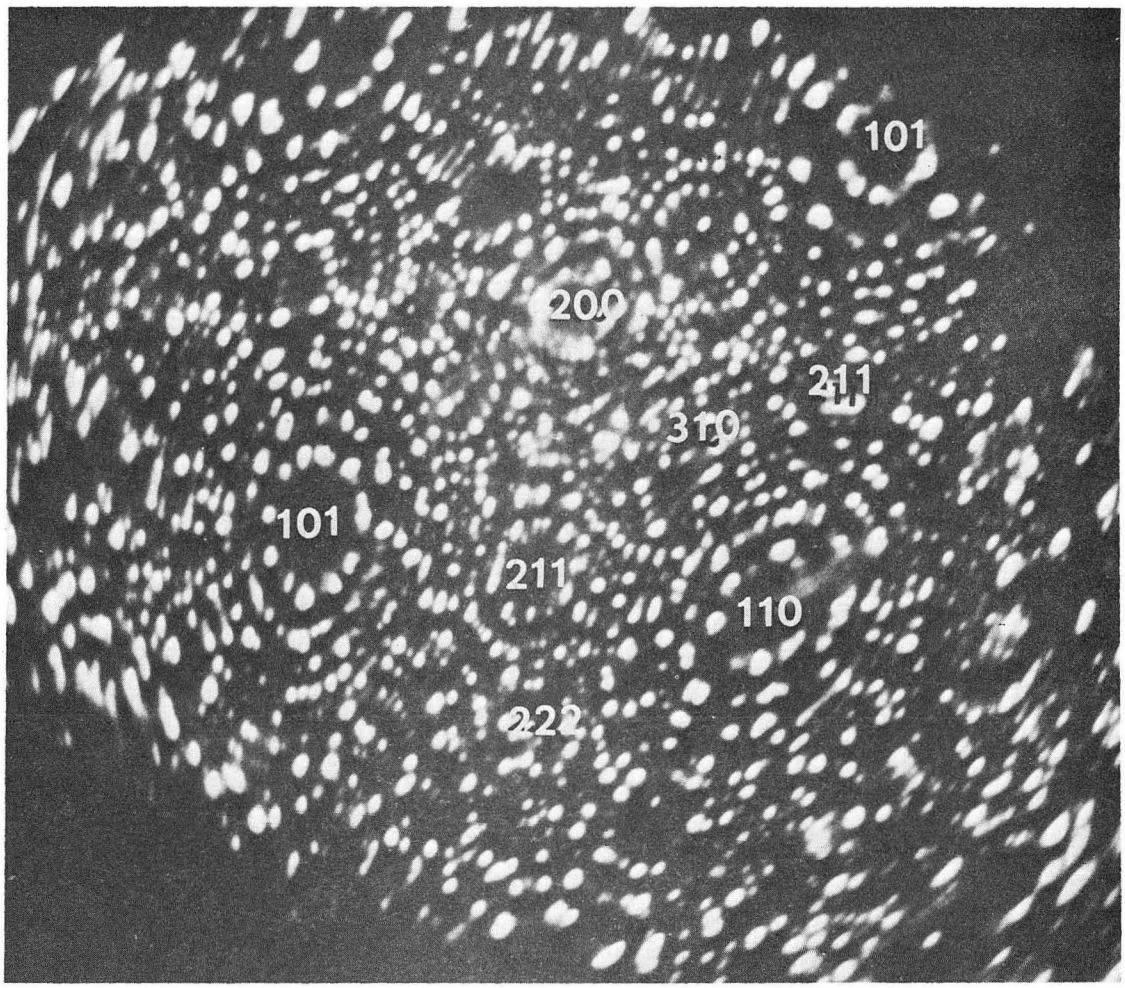

XBB 678-4459

Fig. 20

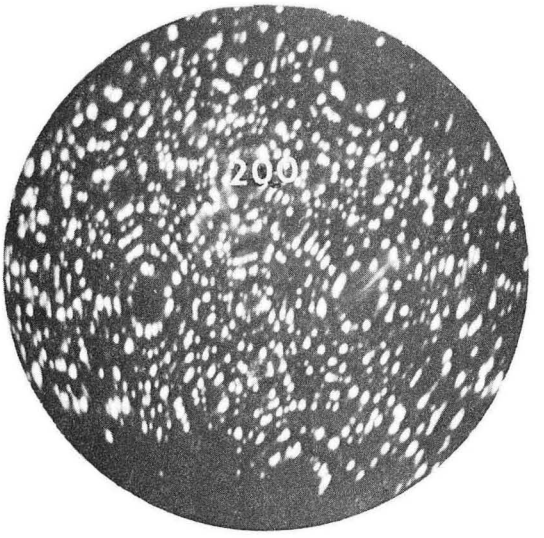

Fig. 21 (a)

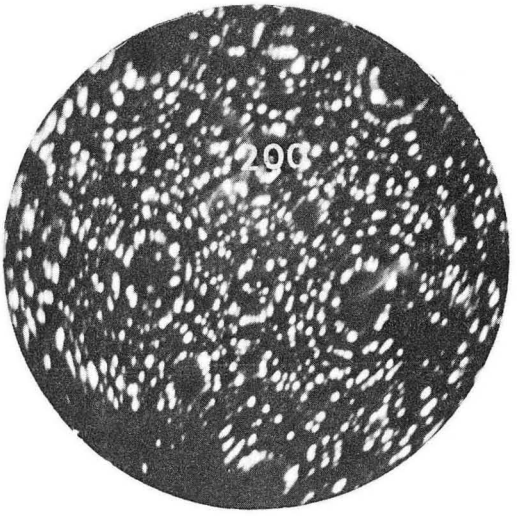

Fig. 21 (b)

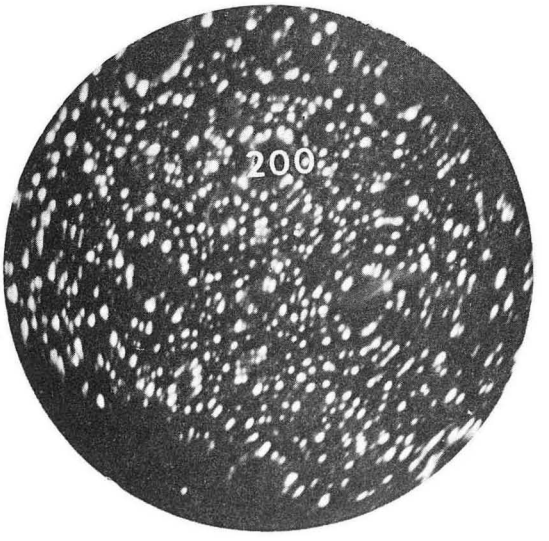

Fig. 21 (c)

XBB 678-4463

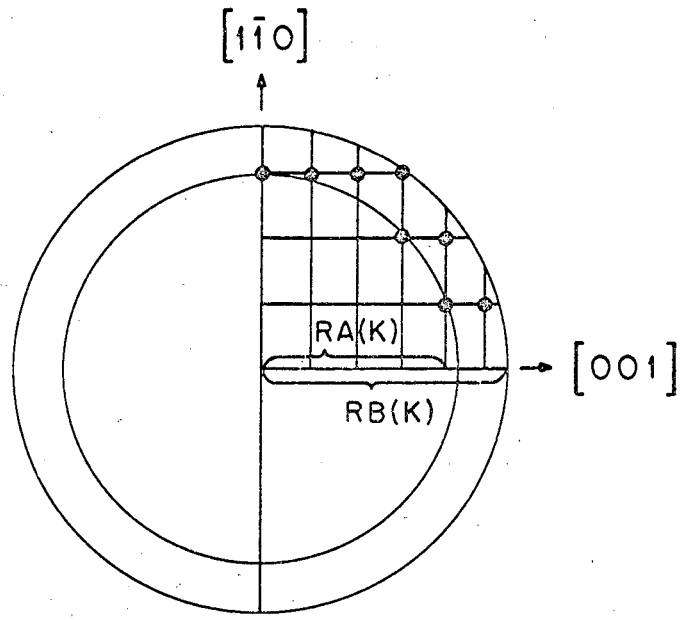

Top view of the ℓ = Kth (110) plane. The lattice points within the annulus are recorded by the computer

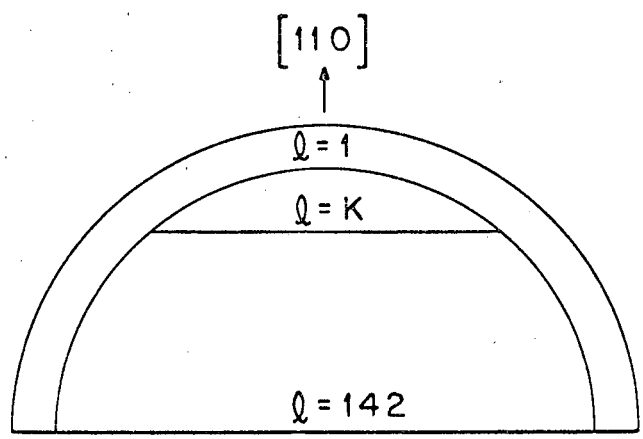

XBL678-3708

Fig. 22

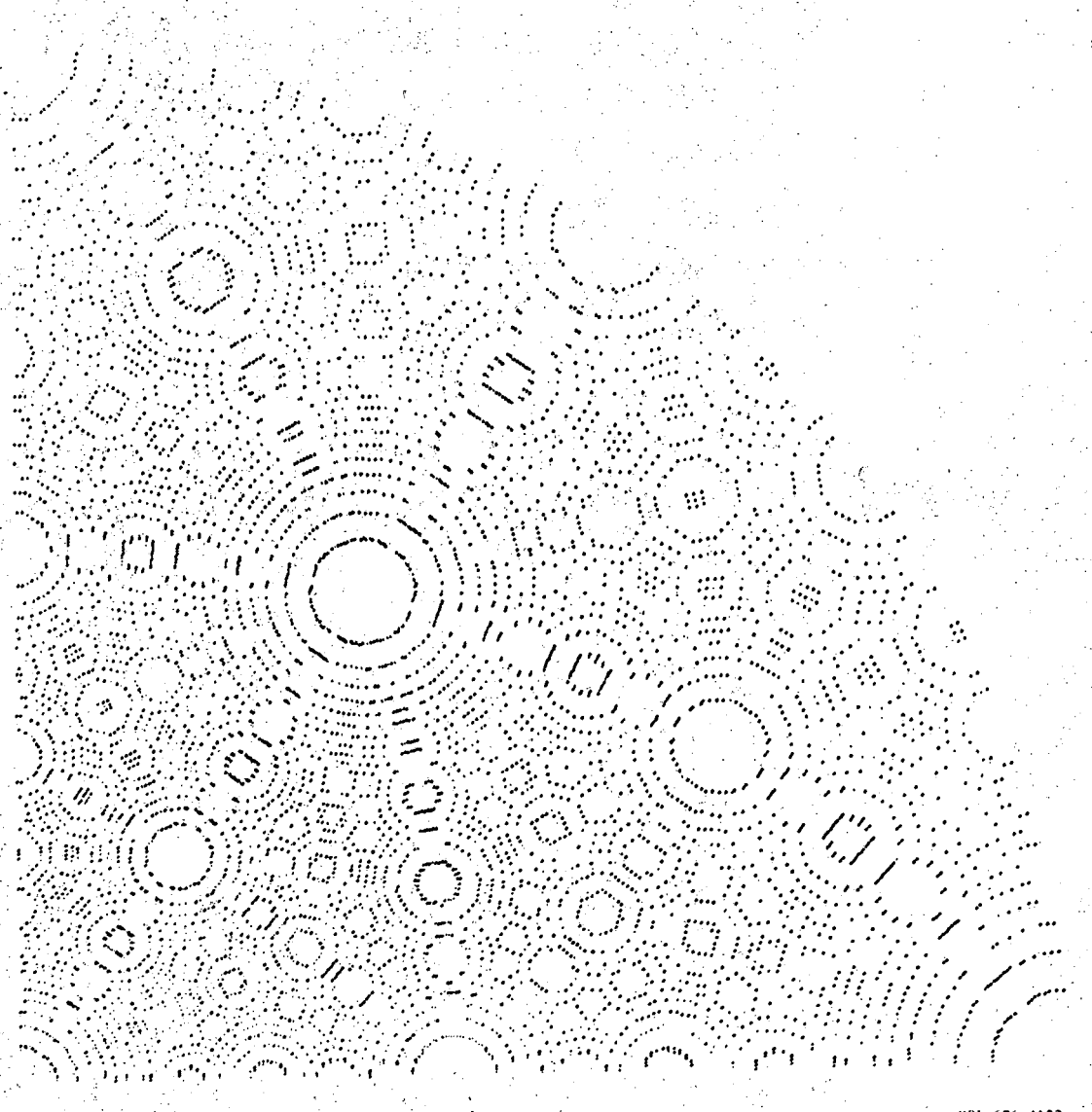

XBL 676-4132

Fig. 23

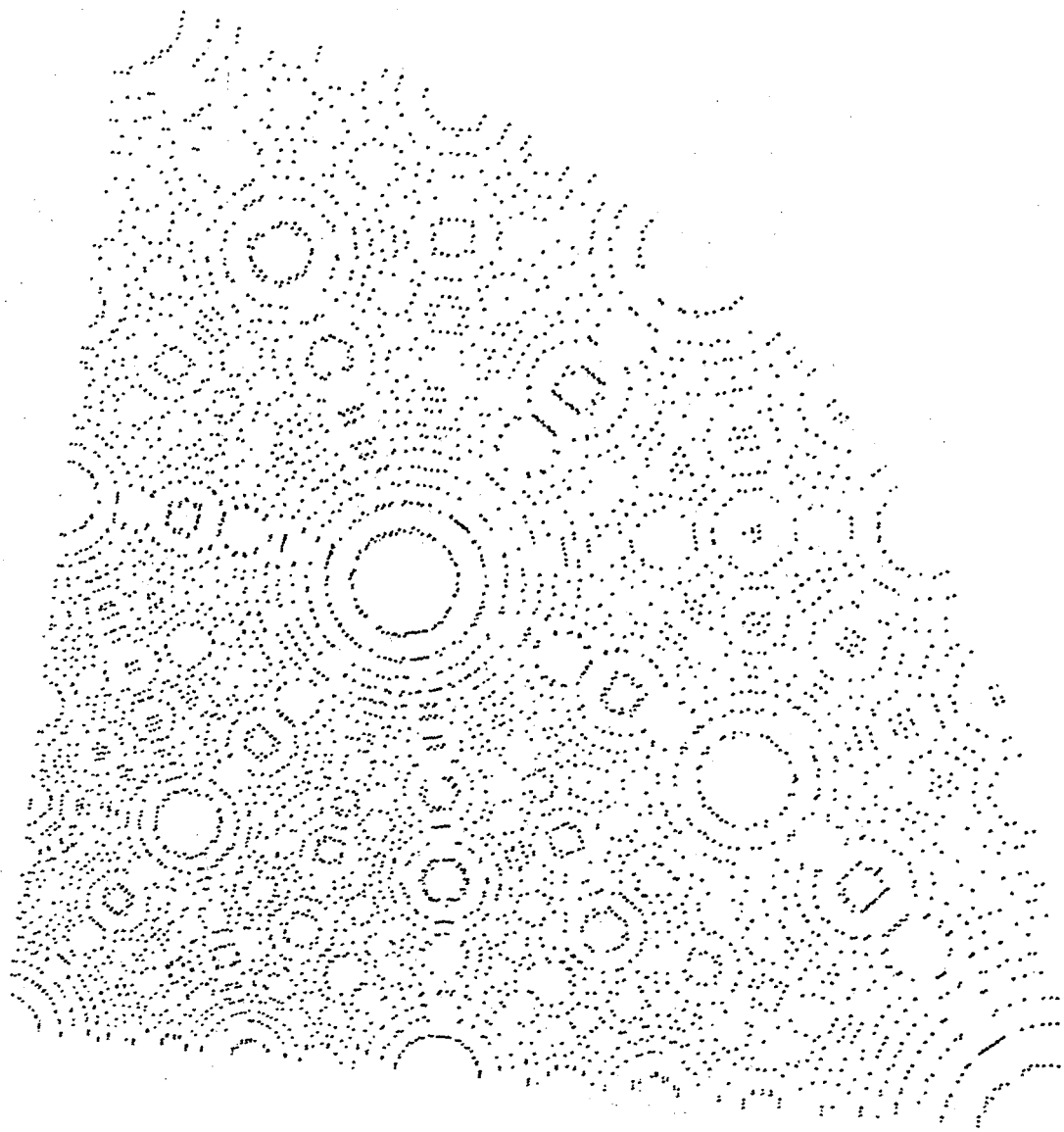

XBL 676-4133

Fig. 24 (a)

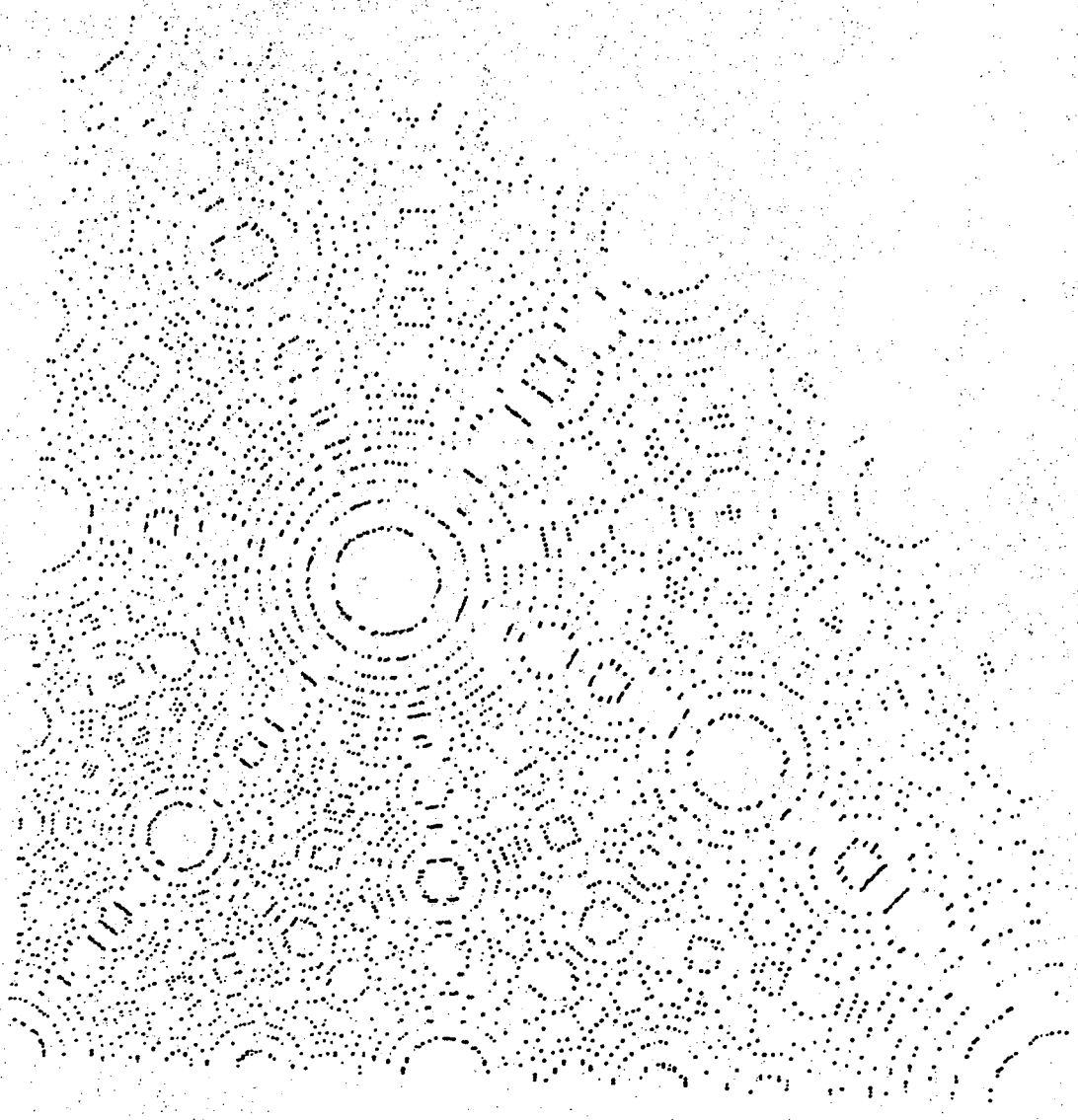

XBL 676-4134

Fig. 24 (b)

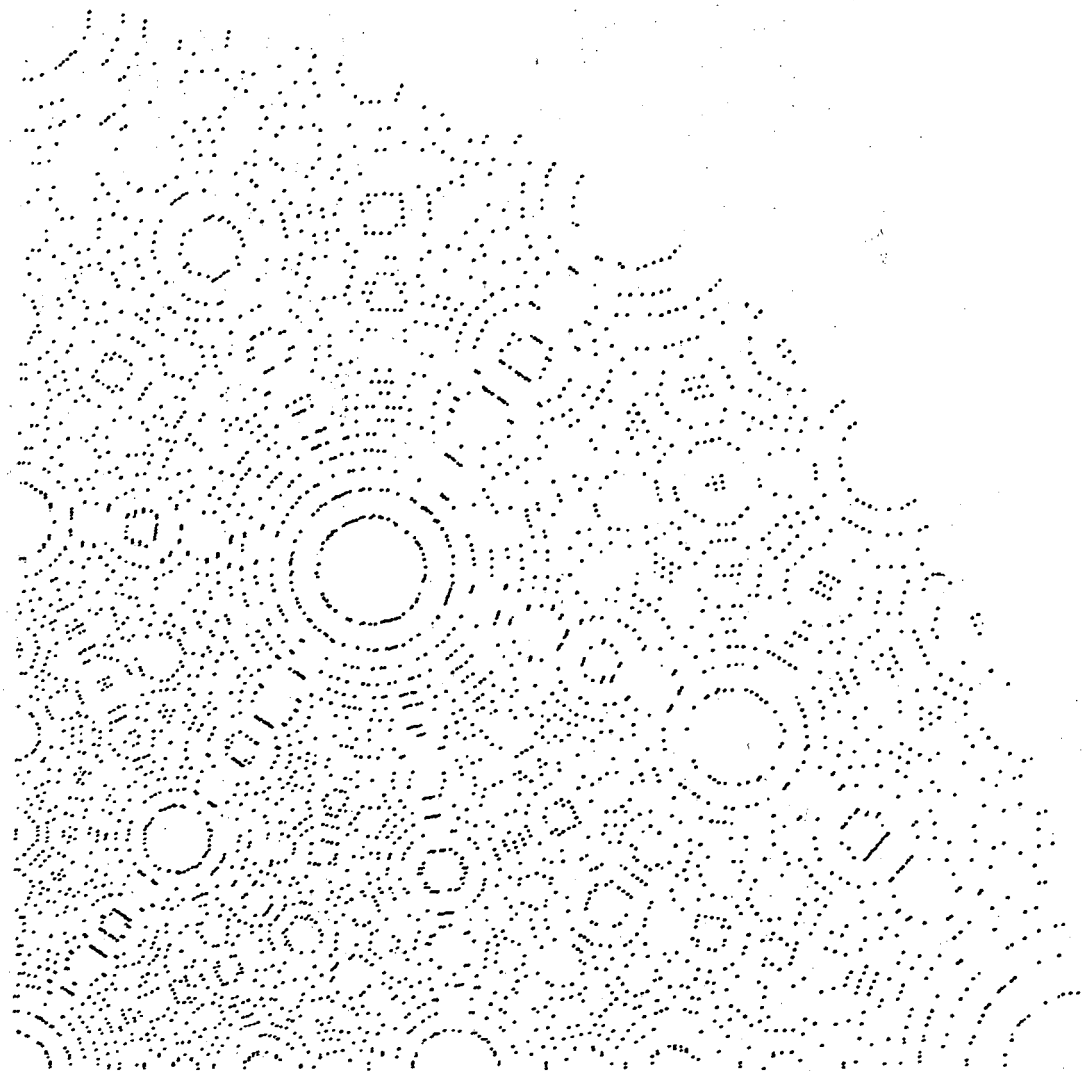

XBL 676-4135

Fig. 24 (c)

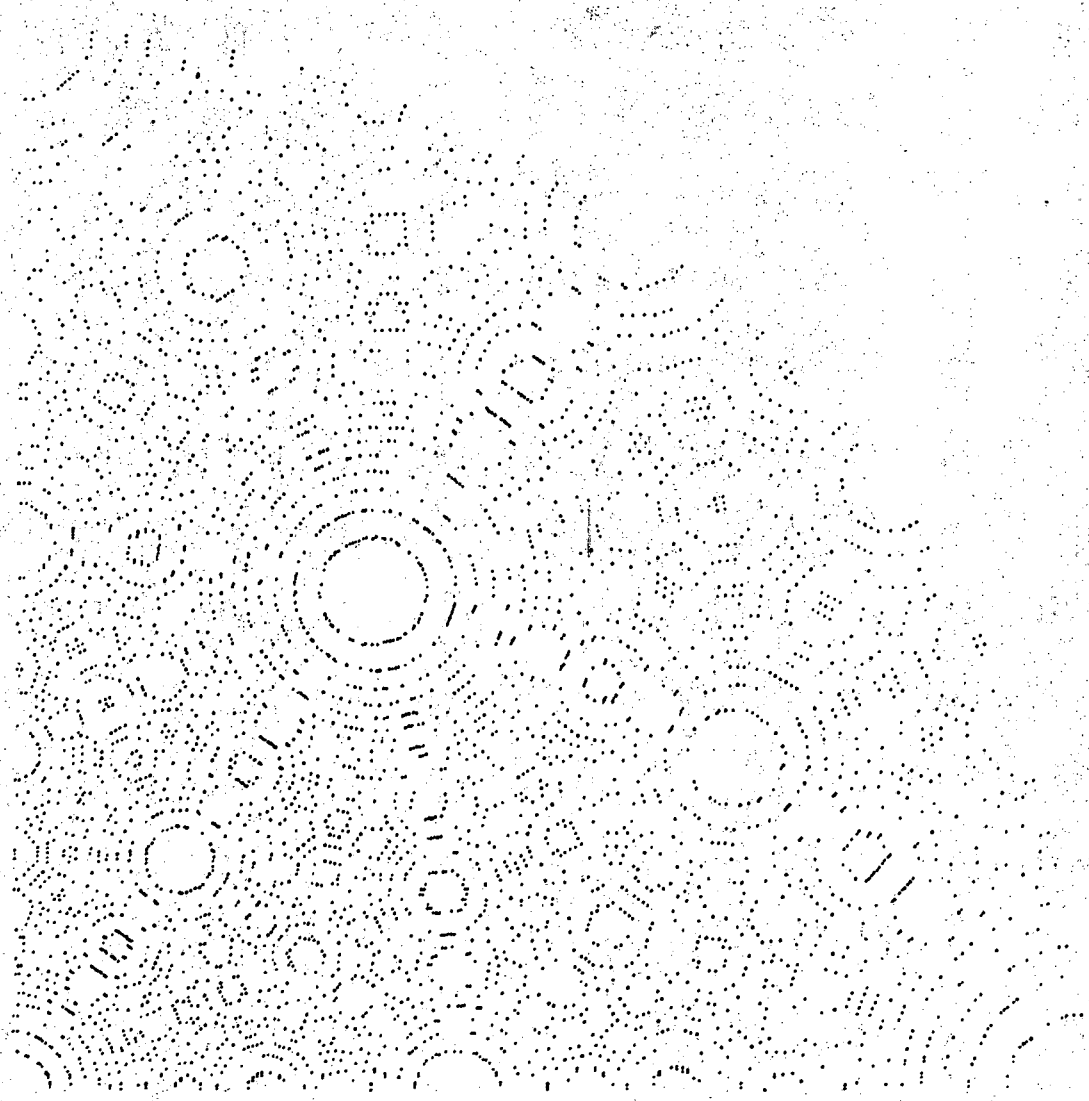

XBL 676-4136

Fig. 24 (d)

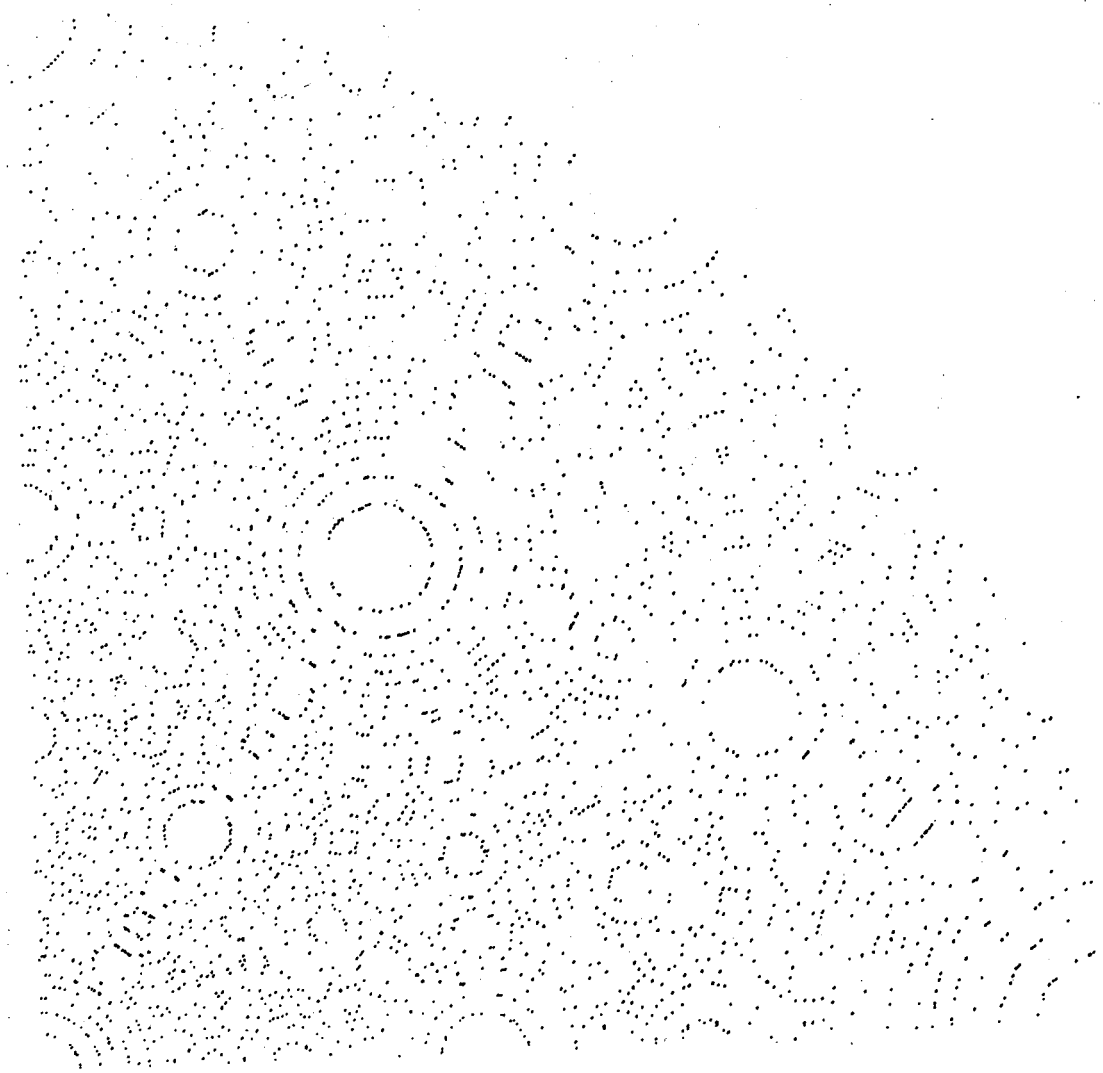

XBL 676-4137

Fig. 24 (e)

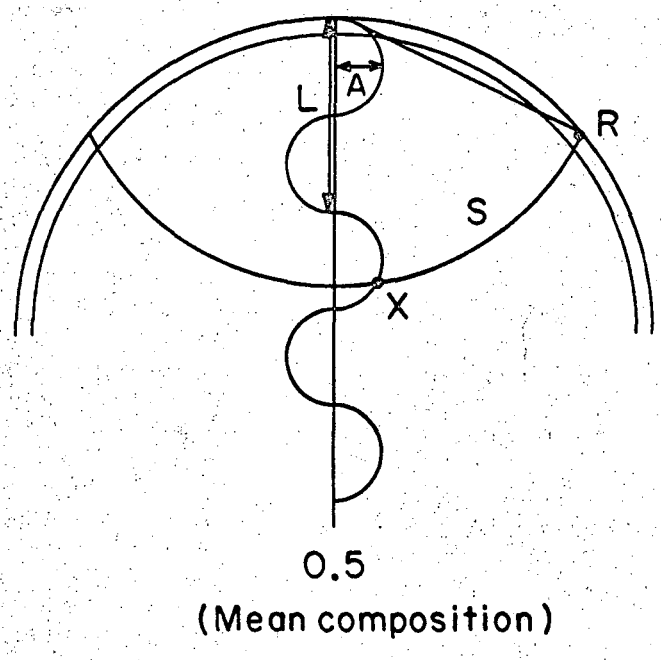

XBL678-3710

R Distance of the lattice point under consideration from the apex

L Clustering period

A Clustering amplitude

S Equicompositional surface with the apex as the center and R as the radius. The composition corresponds to the point of intersection X

Fig. 25

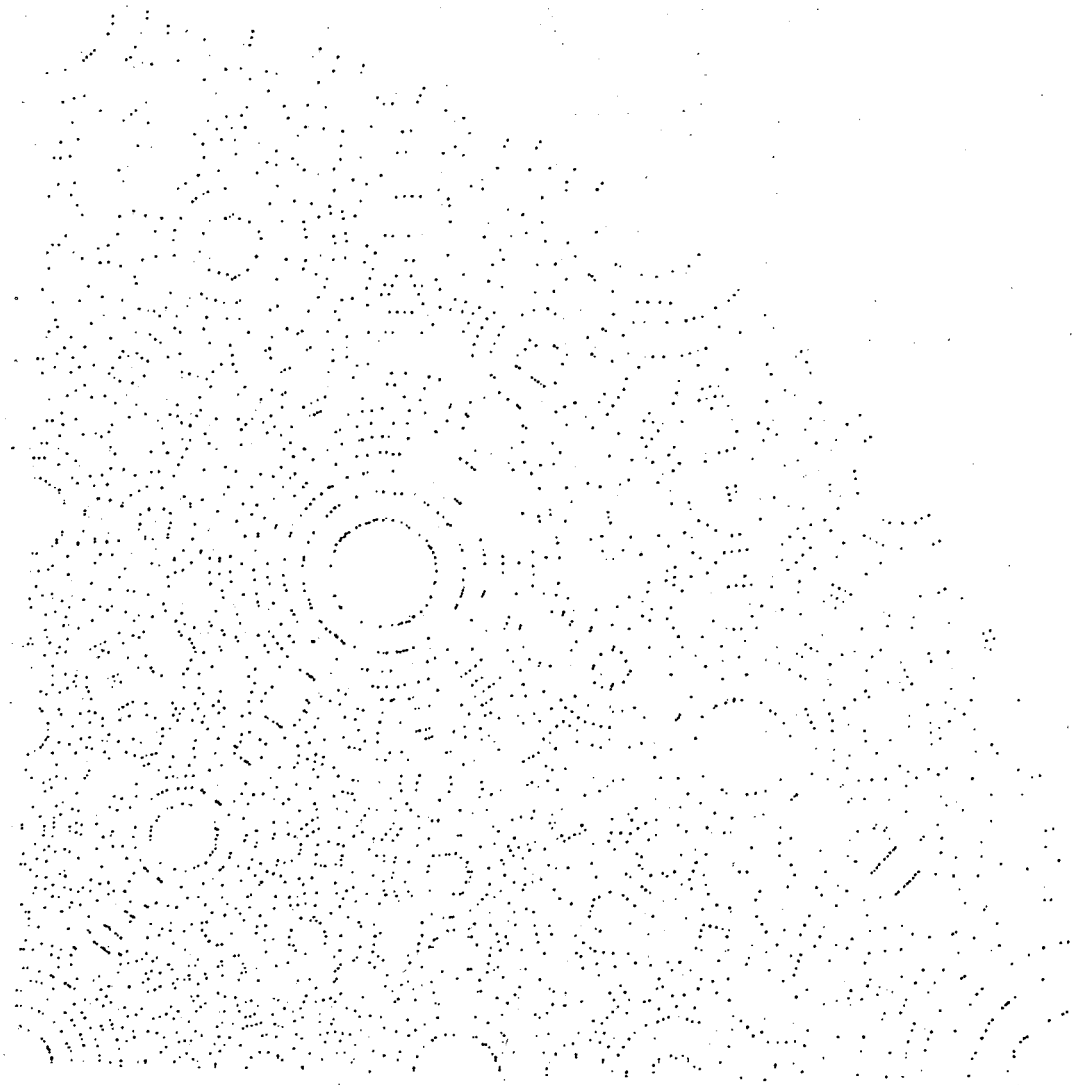

XBL 676-4138

Fig. 26 (a)

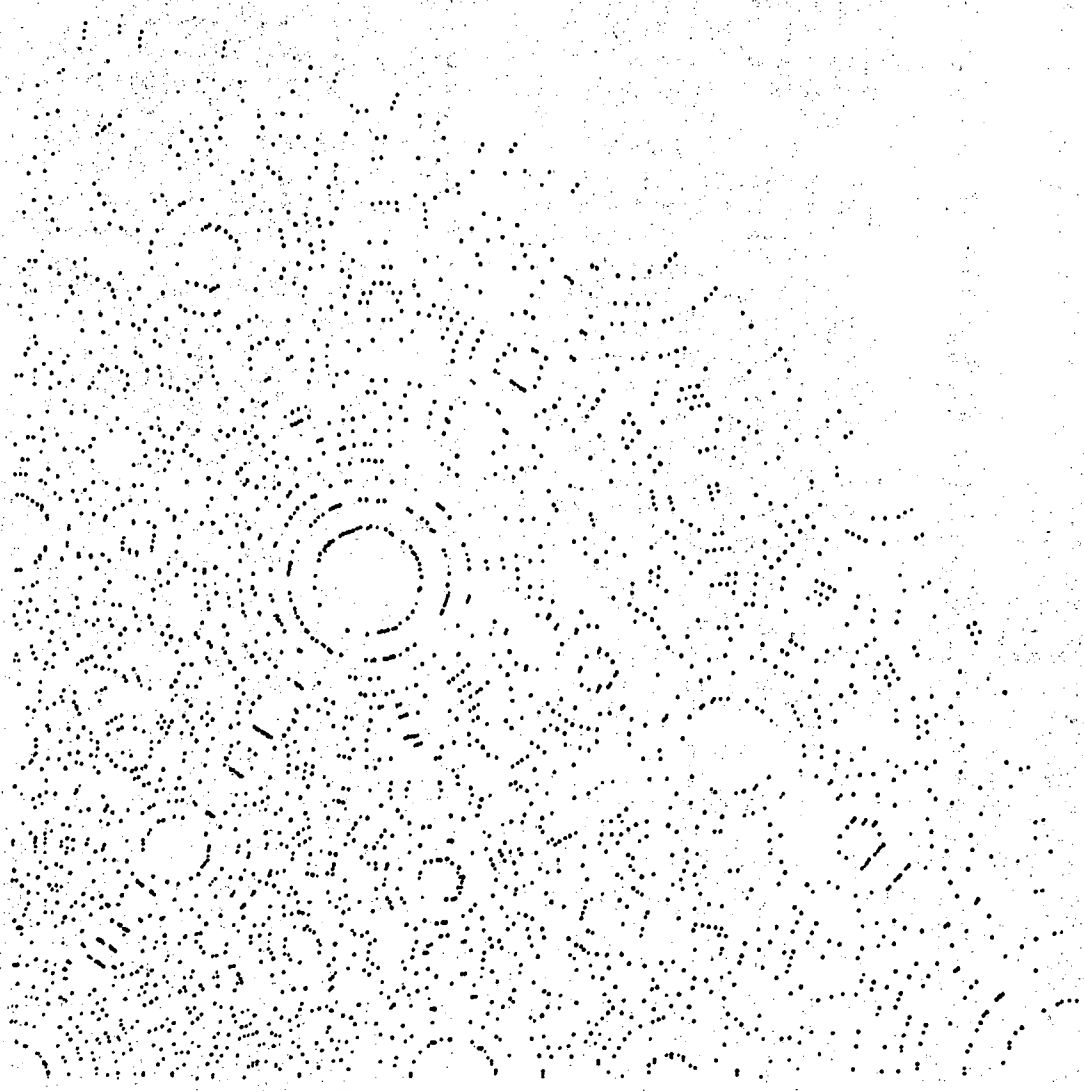

XBL 676-4139

Fig. 26 (b)

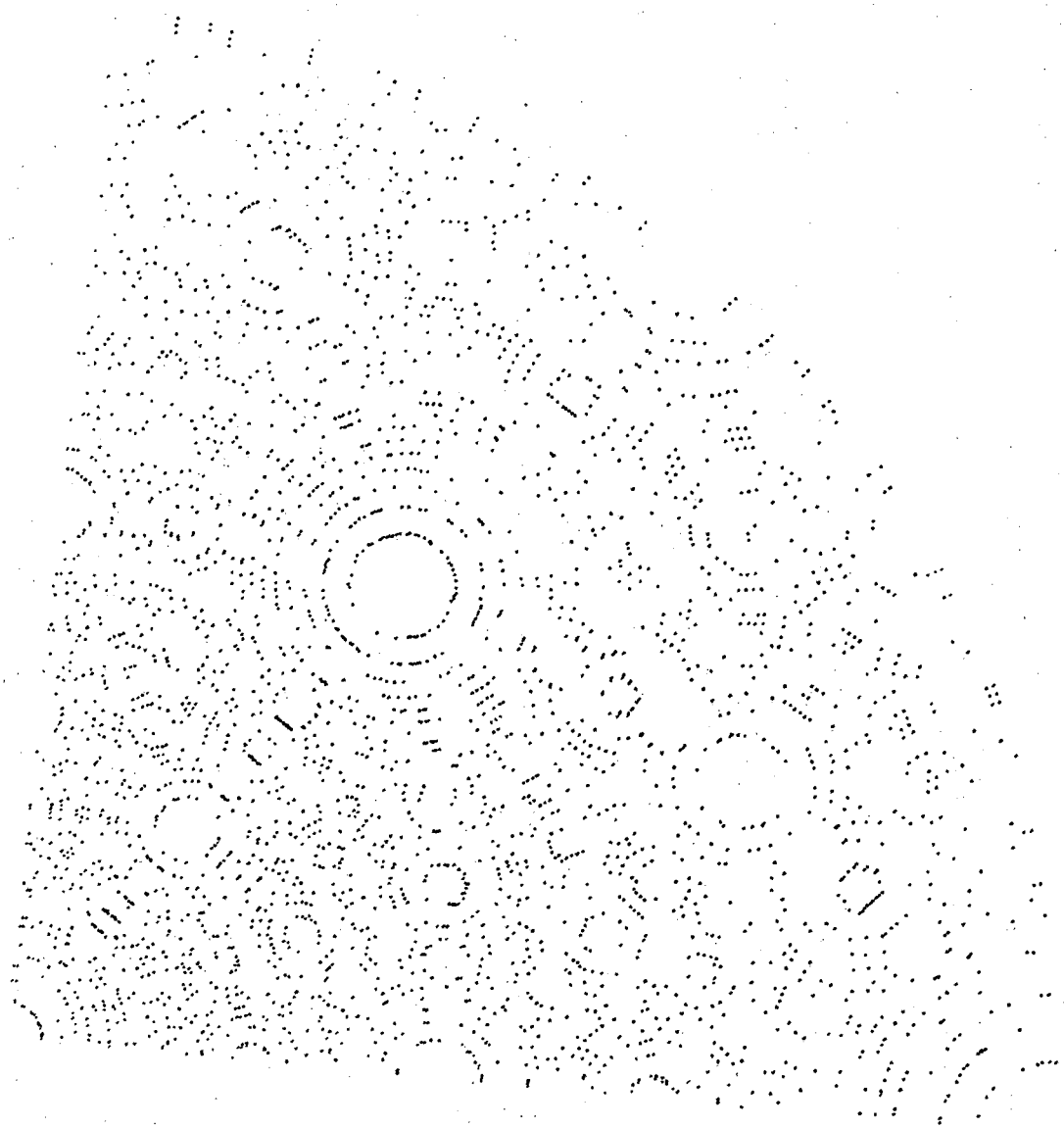

XBL 676-4140

Fig. 26 (c)

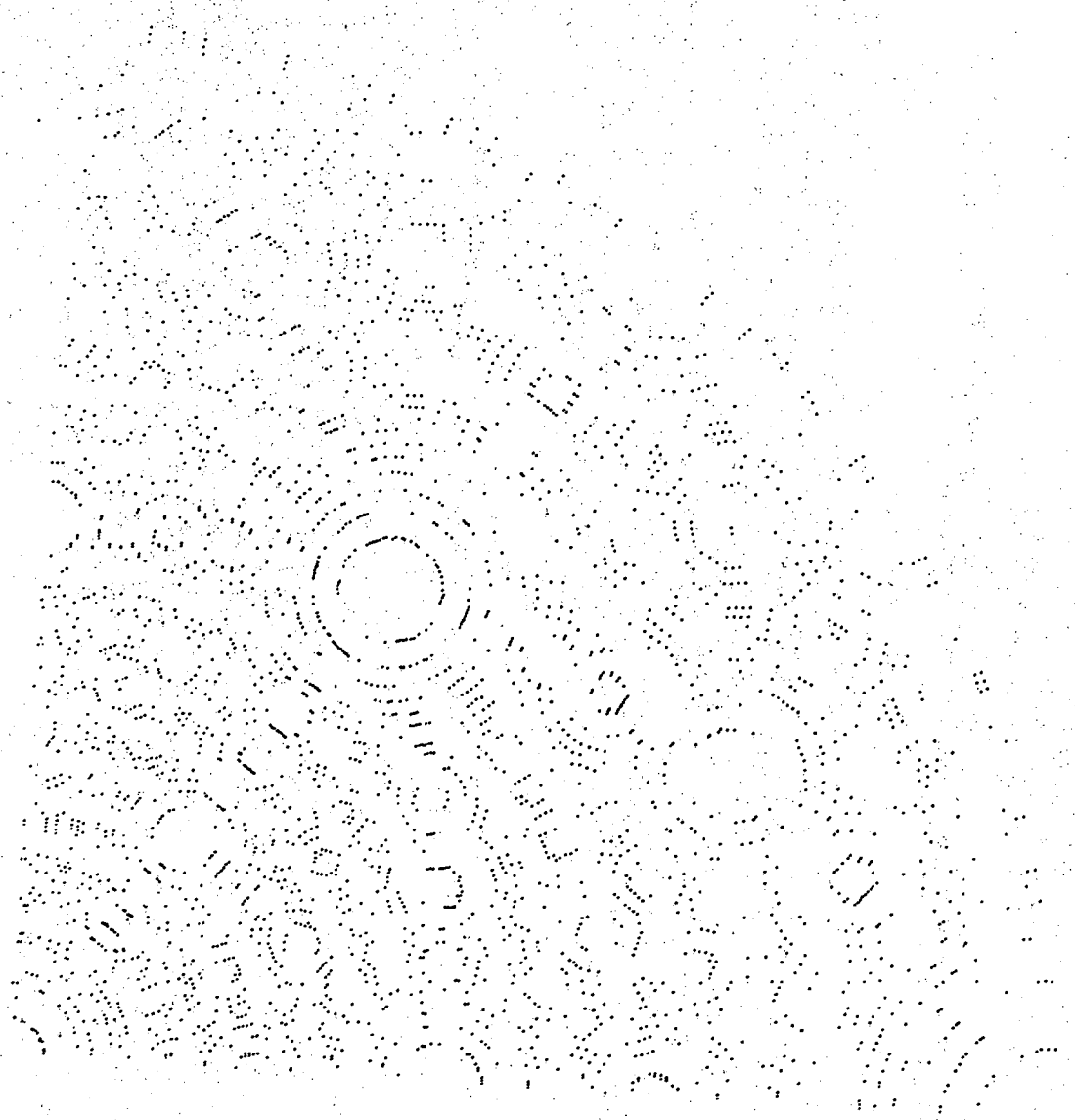

XBL 676-4141

Fig. 26 (d)

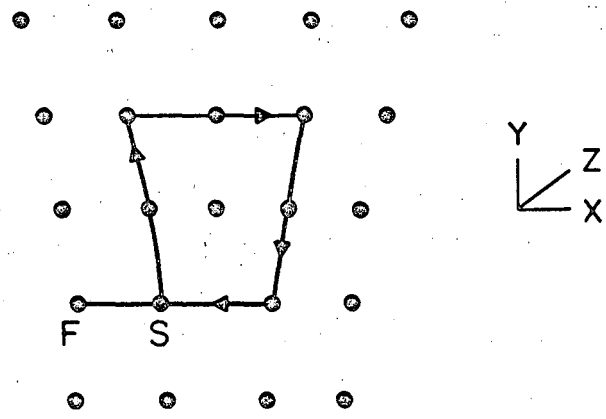

XBL678-3711

The vector FS is the Burgers vector in Burgers notation

Fig. 27 (a)

Spiral contrast: Case $\vec{\ell} \downarrow \uparrow \vec{b}$

A right handed circuit looking at the positive direction. A and B refer to the shank and apex regions of the crystal

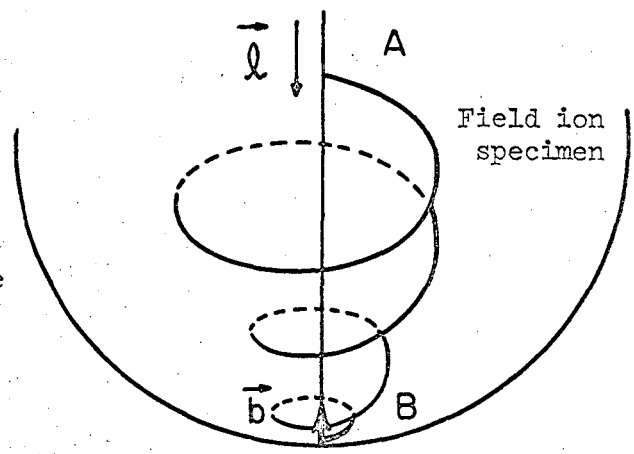

An anticlockwise spiral (with B as reference) on the top of the screen

A clockwise spiral looking through the bottom of the screen as well as on the positive print from the camera

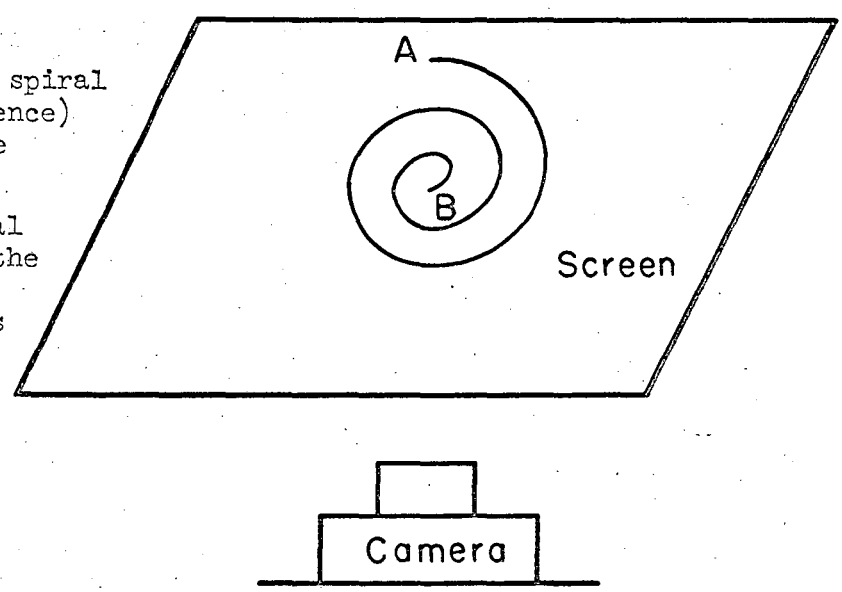

XBL678-3712

Fig. 27 (b)

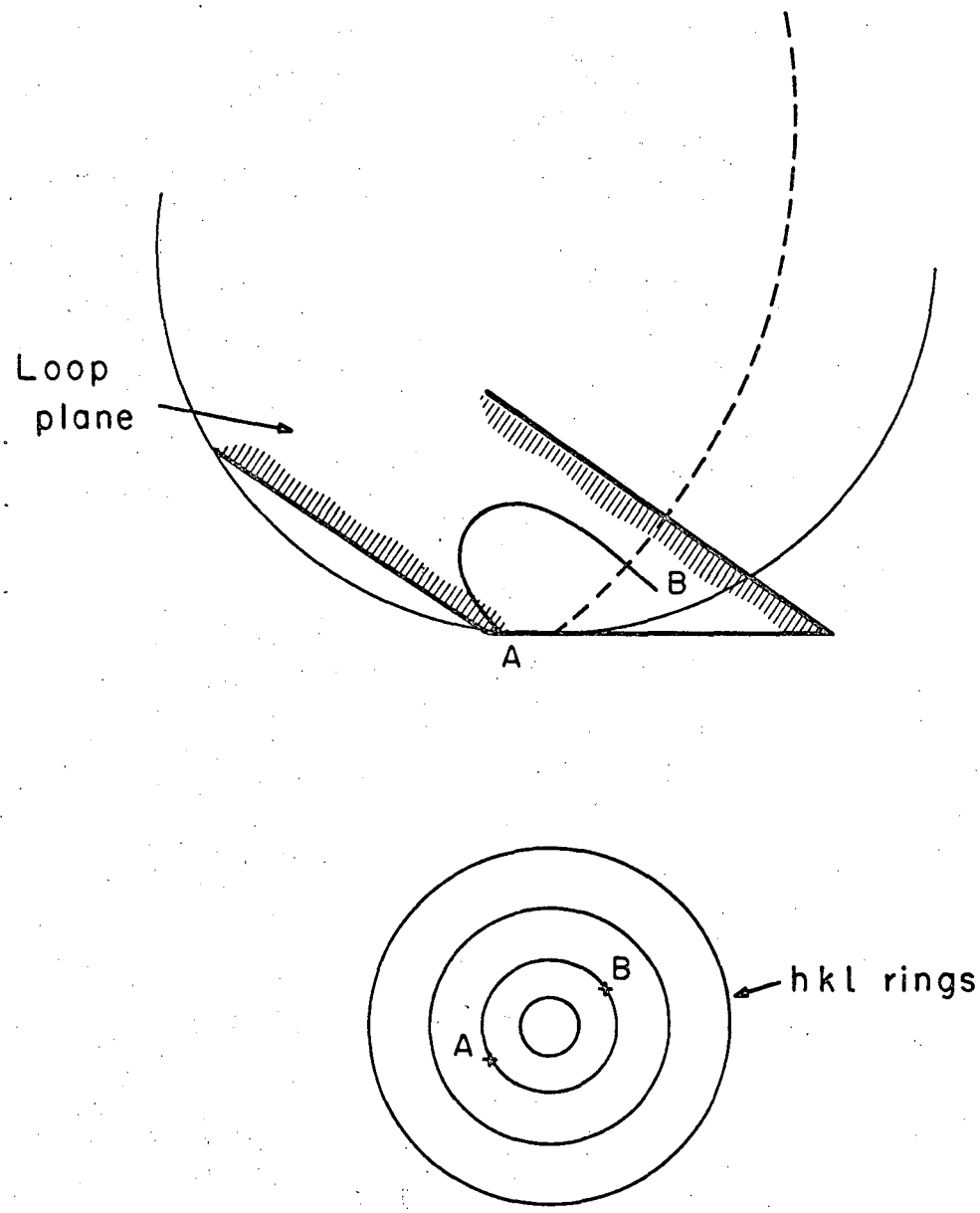

XBL678-3713

Fig. 28 (a)

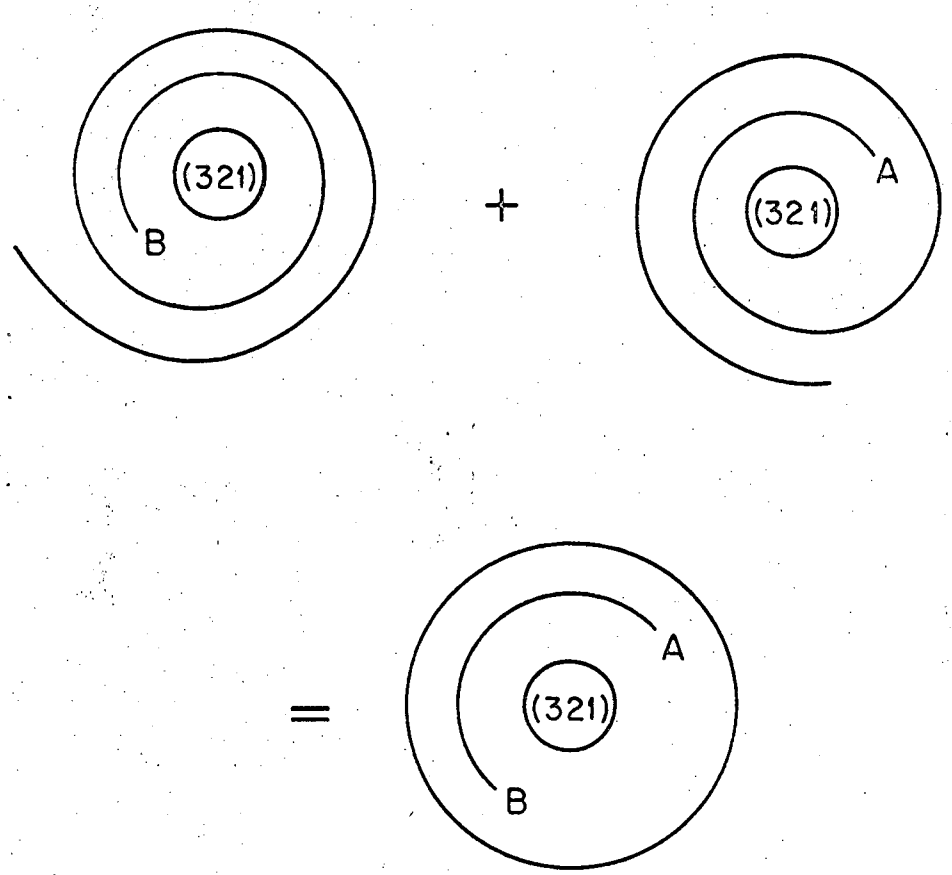

XBL 678-3714

Fig. 28 (b)

This report was prepared as an account of Government sponsored work. Neither the United States, nor the Commission, nor any person acting on behalf of the Commission:

A. Makes any warranty or representation, expressed or implied, with respect to the accuracy, completeness, or usefulness of the information contained in this report, or that the use of any information, apparatus, method, or process disclosed in this report may not infringe privately owned rights; or

B. Assumes any liabilities with respect to the use of, or for damages resulting from the use of any information, apparatus, method, or process disclosed in this report.

As used in the above, "person acting on behalf of the Commission" includes any employee or contractor of the Commission, or employee of such contractor, to the extent that such employee or contractor of the Commission, or employee of such contractor prepares, disseminates, or provides access to, any information pursuant to his employment or contract with the Commission, or his employment with such contractor.